THESIS FOR THE DEGREE OF DOCTOR OF PHILOSOPHY

Optical properties of point defects in insulators and of transition metal dichalcogenides

CHRISTOPHER LINDERÄLV

Cover: Illustration of a defect with associated formation energy diagram and optical spectrum.

Optical properties of point defects in insulators and of transition metal dichalcogenides

Christopher Linderälv
Department of Physics
Chalmers University of Technology

Abstract

There is a need for new or modified materials, both to improve current devices and to create novel functionalities. Engineering materials to target specific functionalities requires a better understanding of how microscopic processes impact materials properties. In this thesis, the effects of defects, mixing of materials, and twisting of parts of the material are explored via first-principles calculations. In particular, the properties of defects in a range of technologically important insulators and of mixing and twisting of transition metal dichalcogenides (TMDs) are addressed, with an emphasis on optical properties.

In the part of the thesis that pertains to defects, the commonality of oxygen vacancies is considered. It is shown that oxygen vacancies exhibit properties that extend beyond specific insulating oxides and that there is a strong interplay between lattice geometry and oxygen vacancy character. The coupling between defect states and lattice vibrations is subsequently accounted for and used to identify the contribution of specific defects to relaxation mechanisms. It is shown that oxygen vacancies may be detrimental to the performance of the oxide phosphor YAG, playing a key role in a reaction mechanism that leads to luminescence quenching. The part of this thesis that is concerned with defects is concluded by an analysis of the optical signatures and phonon sidebands of defects in h-BN and SiC.

On the topic of TMDs, the properties of twisted bilayers are explored, in particular in connection to excitons. It is shown that for very small twist angles, excitons become localized. In addition, the twist-induced potential is dissected and it is shown that the purely electrostatic component of this potential decays with increasing twist angle. Finally, a high-throughput study on TMD alloys was performed for which mixing properties and band edge alignments are presented.

LIST OF APPENDED PAPERS

This thesis is partly based on the author's licentiate thesis (C. Linderälv, *Everything is imperfect: Studies on point defect in insulators* (2020)). It consists of 8 introductory chapters and the following papers:

I   **A Unifying Perspective on Oxygen Vacancies in Wide Band Gap Oxides**
Christopher Linderälv, Anders Lindman, and Paul Erhart
The Journal of Physical Chemistry Letters **9**, 222 (2018)

II   **Luminescence Quenching via Deep Defect States:**
A Recombination Pathway via Oxygen Vacancies in Ce-Doped YAG
Christopher Linderälv, Daniel Åberg, and Paul Erhart
Chemistry of Materials **33**, 73 (2021)

III   **Photoluminescence Lineshapes for Color Centers**
in Silicon Carbide from Density Functional Theory
Arsalan Hashemi, Christopher Linderälv, Arkady V. Krasheninnikov, Tapio Ala-Nissila, Paul Erhart, and Hannu-Pekka Komsa
Physical Review B **103**, 125203 (2021)

IV   **Vibrational signatures for the identification**
of single-photon emitters in hexagonal boron nitride
Christopher Linderälv, Witlef Wieczorek, and Paul Erhart
Physical Review B **103**, 115421 (2021)

V   **Tunable Phases of Moiré Excitons in van der Waals Heterostructures**
Samuel Brem, Christopher Linderälv, Paul Erhart, and Ermin Malic
Nano Letters **20**, 8534 (2020)

VI   **Exciton Landscape in van der Waals Heterostructures**
Joakim Hagel, Samuel Brem, Christopher Linderälv, Paul Erhart, and Ermin Malic
Physical Review Research **3**, 18063 (2021)

VII   **The Moiré Potential in Twisted Transition Metal Dichalcogenide Bilayers**
Christopher Linderälv, Joakim Hagel, Ermin Malic, and Paul Erhart
in manuscript

VIII   **High-throughput Characterization of Transition Metal Dichalcogenide Alloys:**
Thermodynamic Stability and Electronic Band Alignment
Christopher Linderälv, J. Magnus Rahm, and Paul Erhart
in manuscript

The author's contribution to the papers:

   I   The author performed the majority of the calculations and analysis, and jointly wrote the manuscript.

  II   The author performed most of the calculations and analysis, and wrote the first draft of the manuscript.

 III   The author performed a part of the calculations as well as associated analysis and jointly wrote the manuscript.

 IV   The author performed the vast majority of the calculations and analysis, and wrote the first draft of the manuscript.

  V   The author performed and analyzed the first-principles calculations, and contributed to the writing of the manuscript.

 VI   The author performed and analyzed the first-principles calculations.

VII   The author performed the majority of the calculations and analysis, and wrote the first draft of the manuscript.

VIII   The author performed the majority of the electronic structure calculations as well as their analysis and wrote the first draft of the manuscript.

PUBLICATIONS NOT INCLUDED IN THIS THESIS

The following publications are outside the scope of this thesis:

Interlayer exciton dynamics in van der Waals heterostructures
Simon Ovessen, Samuel Brem, Christopher Linderälv, Mikael Kuisma, Tobias Korn, Paul Erhart, Malte Selig, and Ermin Malic
Communications Physics **2**, 23 (2019)

Impact of strain on the excitonic linewidth in transition metal dichalcogenides
Zahra Khatibi, Maja Feierabend, Malte Selig, Samuel Brem, Christopher Linderälv, Paul Erhart, and Ermin Malic
2D Materials **6**, 6669 (2018)

Contents

List of abbreviations

CTL charge transition level. 26, 28, 47–51

DFT density functional theory. 1, 4, 5, 16, 17, 36, 38–40, 42, 43, 45, 48, 52, 54–56

GGA generalized gradient approximation. 38

HR Huang-Rhys. 31–33, 51, 52

LDA local density approximation. 38, 39

LED light emitting diode. 10, 11

PCWLED phosphor converted white light emitting diode. 10, 11

TMD transition metal dichalcogenide. 3, 4, 7, 14, 15, 17, 18, 20, 21, 53–56, 58

vdW van-der-Waals. 14, 39

WLED white light emitting diode. 2, 10

XC exchange-correlation. 37–39, 42

YAG yttrium aluminum garnet. 1, 2, 10, 11, 50

ZPL zero phonon line. 14, 33, 51, 52

1

Introduction

All real crystals have flaws. These flaws disrupt the translational symmetry of the crystal, and present themselves as crystallographic irregularities. And as we have been told symmetries are beautiful, these crystallographic irregularities are called defects. Ruby for example is simply alumina with some atom sites occupied by chromium instead of aluminum atoms. But anybody who has seen a ruby or emerald or another colored gemstone would not think of the impurity atoms that provide the color as a shortcoming of the material.

Diamond with a specific flaw called the NV^{-1} center, is investigated as a potential corner stone in emerging quantum technologies. For example, it has been demonstrated that two NV^{-1} centers in the vicinity of each other can be used to form entangled states [1], which is the fundamental unit required in many quantum information technologies. This is only one of many systems where defects provide a functionality of a material that is absent in the pristine material. In fact, defects in solids have emerged to be one of the most promising platforms for creating and studying quantum phenomena such as single photon emission [2]. Over the last century, research and development has proven that for numerous materials it is the defects that make the material useful in certain applications with examples including oxides such as yttrium aluminum garnet (YAG) [3], silicon carbide [2] and hexagonal boron nitride (h-BN) [4]. Therefore, the study of defects in materials is of outmost importance with regard to the development of materials for future applications.

The size of a point defect is comparable to the size of an atom and such defects are hence difficult to probe with experiments. First-principles calculations are therefore crucial in order to understand the impact of specific defects on the materials properties. However, first-principles calculations on defects in insulators are very demanding since large supercells are required to embed the defect. Furthermore, conventional density functional theory (DFT), which is the most feasible alternative, has several shortcom-

ings in describing charged defects in insulators [5]. In this regard, it is important to address the question as to how transferable properties of defects across materials are. If certain properties are transferable, assessing the impact of defects in different materials would be easier and screening of materials for certain functionalities would require less resources. It is not expected that any defect in any material exhibits the same behavior, yet specific defects across similar materials may. In particular, we focused our attention on wide band gap oxides and addressed the following question in **Paper I**.

> **Q1**. Is it possible to understand the properties of oxygen vacancies in wide band gap oxides without having to explicitly study the oxygen vacancy in each new oxide?

In order to be able to follow **Paper I**, a chapter that is devoted to the general theory of defects in solids (Chapter 3) is included in this thesis. Additionally, to explain the common features of the considered oxides in **Paper I** a section on the electronic structure of wide band gap oxides is included (Sect. 2.1.1). It turns out that one characteristic feature of oxygen vacancies in many materials is a large structural relaxation in connection with a change in charge state. This implies that when the oxygen vacancy gains or looses an electron, a considerable amount of energy is dissipated in the form of lattice vibrations.

So far the focus has been on positive effects of defects. There are however numerous common adverse processes in materials that are related to the presence of defects. The chemical nature of the defects is often elusive, which can make it difficult to design synthesis strategies to prohibit the formation of these defects by other means than trial-and-error. One such adverse process is the thermal quenching in oxide phosphors seen in, e.g., Ce doped YAG, which is a yellow phosphor widely used in white light emitting diodes (WLEDs) [3]. Here, the thermal quenching has been attributed to defects without any further specification [6, 7]. With the large energy dissipation potential of oxygen vacancies in mind we therefore asked the following question in **Paper II**.

> **Q2**. Can oxygen vacancies provide the missing link in a complete microscopic description of luminescence quenching in Ce-doped YAG?

In **Paper II**, we propose a non-radiative charge transfer mechanism that involves oxygen vacancies. To provide background for this paper, there is a section on solid state lighting that covers luminescence quenching (Sect. 2.1.1.3). Additionally in **Paper II**, we modeled the fine structure (lineshape) of the optical transitions on the Ce atom using the generating function method (Sect. 3.3.2). This is a method that accounts for the change in vibrational state upon a change in the electronic state. The method was conceived in the 1950ies [8] but has in recent years experienced a renaissance as it has become easier to compute the vibrational spectrum of large defective supercells due to more powerful computers as well as better methods and algorithms [9–11]. In particular, this method accounts for the structural distortion associated with a transition on a defect, which

makes the method a suitable tool for extracting optical fingerprints of defects. This is especially relevant for materials such as h-BN and SiC, which are of interest as hosts for single-photon emitters similar to the case of the NV^{-1} center mentioned above. In fact, in **Paper III** and **Paper IV** we worked with the following question.

> **Q3**. Can we model the optical lineshapes and identify defects based on observed emission lineshapes?

Paper III is concerned with color centers in SiC and in **Paper IV** we directed our efforts to identifying defects in 2D h-BN. A more detailed description of these materials and defects is presented in Sect. 2.1.2. **Paper IV** marks the end of the part of this thesis that is concerned with defects in wide band gap materials and provides a bridge to the realm of 2D materials, which is the subject of interest in **Paper V**-**Paper VIII**.

While defects can add functionality to a material, there are additional ways to modify and change the materials properties. Some materials that exhibit a layered structure, e.g., MoS_2 and graphite, have been shown to exhibit a profoundly different electronic structure in the monolayer limit [12, 13]. MoS_2 is an indirect semiconductor in bulk form, which undergoes a transition to a direct band gap semiconductor in the monolayer limit. In graphite, the band gap vanishes in the monolayer limit (graphene) and the electronic states around the Fermi energy become massless [14]. Graphene has shortcomings when it comes to optoelectronical applications due to the vanishing band gap and therefore the semiconducting transition metal dichalcogenides (TMDs) such as monolayer MoS_2 are better suited for applications in this field.

The optical properties of TMD *monolayers* have been extensively studied, both via experiments [15] and theory [16]. Overall, there is a good understanding of the exciton formation and dynamics in monolayers. Excitons in *bilayers*, however, are a much more complex subject due to interlayer coupling and potential band offsets between the monolayers. This gives rise to intralayer excitons that are confined to a single layer and interlayer excitons for which hole and electron reside in different layers. The subject is further complicated by the presence of combinations of these two types of excitons as well as the twisting degree of freedom available in moiré structures.

The optical properties of TMDs and in particular twisted bilayers are the subject of the final part of this thesis. Twisted bilayers have received a lot of attention in recent years and exhibit peculiar properties that are very distinct from those of their untwisted counterparts [17]. In **Paper V** we therefore investigated the following question.

> **Q4**. How are the optical properties of a TMD bilayer affected by twisting one of the constituent monolayers?

In order to understand the concepts in this study, a section on TMDs is included in Sect. 2.2.1 where general properties of TMDs are introduced. One inherent property

of unstrained twisted bilayers is that the unit cell gets prohibitively large for low twist angles. In **Paper V**, this issue was addressed by using a methodology based on density matrix theory [18] in combination with DFT+*GW* calculations on a model system that mimics the twisted bilayer in the low angle limit by considering bilayer unit cells with different stacking orders.

Bilayers with different stacking orders are interesting in themselves. In **Paper VI**, we therefore considered excitons in bilayers for different stacking orders. This study was performed with the outlook of predicting how the exciton properties vary for different TMD material combinations and stacking orders. Furthermore, an important objective of **Paper VI** was to address the following question.

> **Q5**. Is it possible disentangle the effects of electric potential and level hybridization on the energy levels of the bilayer?

The importance of this question resides partly in the prospect of creating more complex models to enhance the understanding of exciton properties in twisted bilayers. The model used in **Paper V** is as already stated limited to low twist angles. In this regard, we considered explicit moiré supercells in **Paper VII** and addressed the following question regarding the twist-induced potential (moiré potential).

> **Q6**. What are the origins of the moiré potential, and how can we access very small (non-zero) twist angles?

In order to see how the low-angle-limit model is related to twisted bilayers with a finite twist angle, a section on the construction of explicit moiré supercells is included here (Sect. 2.2.3). While it was not possible to extract excitation spectra of twisted bilayers in **Paper VII**, additional insights concerning the fundamental properties of the moiré potential were obtained, namely that the potential arises due to a stacking dependent charge density displacement upon bilayer formation.

While twisting allows one to manipulate a material without changing the chemical constituents of the material, it has a rather limited effect of the overall electronic structure. In order to tailor the position of the band edge states over a wider energy range, which is desirable for applications in , e.g., optoelectronics and catalysis, one requires more drastic means. In **Paper VIII** we therefore address the following question.

> **Q7**. Besides twisting, what additional ways are there to engineer the optical properties and in particular the position of the band edges?

We direct our focus on alloying and in particular the mixing ability of TMD monolayer alloys and the alignment of the band edges. To this end, a section on thermodynamics of binary alloys is included (Sect. 2.2.4). **Paper VIII** concludes the studies that have been performed within the scope of this thesis.

Most of the data in **Paper I**-**Paper VIII** has been generated using first-principles calculations based on DFT. Therefore, a chapter on first-principles calculations (Chapter 4) is included in this thesis as well.

2

Background

This chapter provides background for the appended studies. First, defects in wide band gap materials are introduced (Sect. 2.1), which creates context for **Paper I**-**Paper IV**. In the second part (Sect. 2.2), TMDs are introduced, which is relevant for **Paper V**-**Paper VIII**.

2.1   Defects in wide band gap materials

2.1.1   Oxides

Oxygen forms compounds with basically every other element in the periodic table. Wide band gap oxides is a rather large class of oxides and not uniquely defined. Here, we define them as oxides with band gaps above ≈3 eV. We furthermore restrict ourselves to crystalline materials. The valence electron configuration of oxygen is $2s^2 2p^4$. In the *ionic limit* oxygen occurs as a doubly negatively charged ion with a closed valence shell $2s^2 2p^6$ in binary metal oxides. In the case of a completely depleted metal valence shell, which is reflected in the stoichiometry of the oxide, the valence band consists of oxygen $2p$ states and the conduction band of unoccupied metal states.

2.1.1.1   Electronic structure

The type of a semiconductor/insulator can often be classified according to the predominant character of the valence and conduction bands. While the degree of covalency can be relatively large, it is still useful to keep the notion of anion and cation, and it is usually possible to distinguish the *main* contributions to the valence band and conduction bands.

An open shell semiconductor or insulator for which the valence band is dominated by anion states and the conduction band by cation state is said to be a charge trans-

fer semiconductor or insulator. Here, the *charge transfer* refers to the fact that the lowest electronic excitation involves a charge transfer between anions and cations. When both valence and conduction band are predominantly composed of cation states, the semiconductor or insulator is of Mott-Hubbard type and the lowest excitation involves charge transfer between cations.

In 1985, Zaanen, Sawatsky, and Allen developed a theory in order to qualitatively understand the electronic structure of transition metal compounds applicable to binary transition metal oxides [19]. In the Zaanen-Sawatsky-Allen theory a distinction between charge transfer and Mott-Hubbard insulators can be made. The theory is simple in the sense that it is based on only three material specific parameters to describe the type of insulator. The essence of the Zaanen-Sawatsky-Allen theory is that the electronic properties of an ionic transition metal oxide are dependent on the charge transfer energy between the oxygen and metal states (δ) and the correlation energy between the metal states (U) (Fig. 2.1a). The third parameter entering the Zaanen-Sawatsky-Allen theory is the oxygen $2p$ bandwidth.
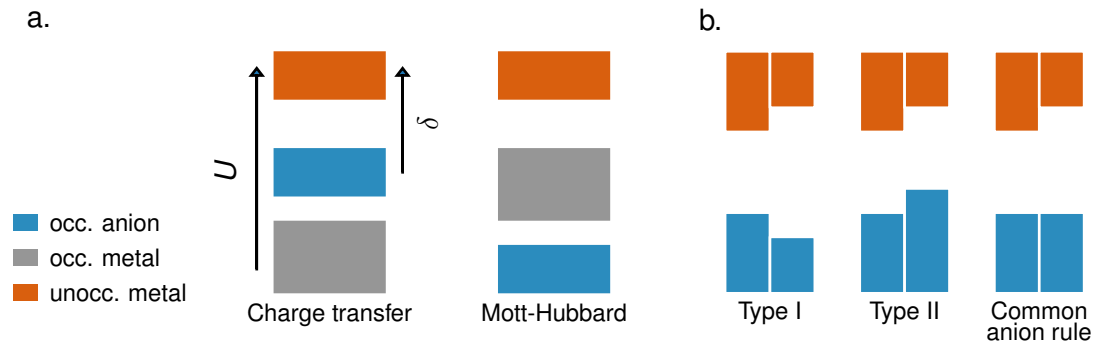
Figure 2.1: a) Illustration of the parameters for the Zaanen-Sawatsky-Allen theory. The blue color indicates the occupied anion band whereas the gray color indicates occupied cation states and the red color indicates unoccupied cation states. The difference between the band edge character in charge transfer insulators and Mott-Hubbard insulators is indicated. b) Schematic illustration of band alignment of two compounds. The two common band alignments; type I and type II are shown as well as an intermediate alignment corresponding to the common anion rule.

Mott-Hubbard insulators have $\delta - U > 0$, while for charge transfer insulators $\delta - U < 0$. The binary transition metal oxides studied in the publications that this thesis is based on are closed shell oxides. As such, the unoccupied metal states are usually well separated from the occupied oxide states, *i.e.*, $U \gg \delta$ [20].

The relative band edge positions between different materials are important in any device that includes a heterojunction of these materials. Therefore, extensive efforts have been made in order to understand how band edges align in heterostructures. There are two main types of alignment, type I and type II (Fig. 2.1b). In type I aligned materials, both band edges belong to the same material, so that an excitation predominantly

occurs within the same material, whereas in a type II aligned heterostructure the valence band edge and conduction band edge belong to different materials. In binary ionic closed shell insulators, the anion valence states are occupied and the cation valence states are unoccupied in the ground state. It has been observed that compounds with common anions tend to exhibit a much smaller variation of the valence band edge position in comparison with the conduction band edge [21] (Fig. 2.1b). This observation is the basis of the so called common anion rule. The common anion rule states that the valence band edge position is *primarily* determined by the energy level of the anion valence state, whereas the conduction band edge position is primarily determined by the energy level of the cation valence state. Wei and Zunger showed that the common anion rule breaks down when cation states mix with anion valence band edge states [22].

2.1.1.2 Defects

Defects are particularly important in oxides proposed for applications involving electronic transport. Examples of oxides that fall in this class are ZnO, In_2O_3, SnO_2, β-Ga_2O_3, $BaSnO_3$ as well as $CuAlO_2$ [23–25].

In order to take full advantage of wide band gap oxides, it is necessary to develop p-doped oxides, and so far it has been difficult to achieve p type doping in binary closed shell wide band gap oxides. These oxides are generally easier to n-dope and realizing p-doped oxides has been a long standing research objective [26]. The origin of the preferred n-doping over p-doping is believed to be related to the formation of oxygen vacancies which act as electron donors in many oxides, though the donor efficiency of the oxygen vacancy varies between materials [27].

The main difficulties involved in utilizing p-doped oxides can be understood by first considering the O^{2-} ion, which is a closed shell ion and is unlikely to host a free hole. Secondly, if one manages to form O^- (peroxide) ions, hole capture by occupied abundant intrinsic hole killers reduces the hole concentration. And even if an oxide with a valence band of $2p$ states, e.g., ZnO and In_2O_3, could be easily p-doped, the effective mass of the hole is usually very large. As a result, the free hole mobility for the cases where the valence band edge consists of oxygen $2p$ states is very low, which limits the usefulness in electrical devices [28, 29]. Finally, it has also been shown that holes may form small polarons (self trapped holes) in the oxides SnO_2, Ga_2O_3, and In_2O_3, which further reduces the hole mobility [30] in these materials.

Intrinsic hole killers in oxides have been widely studied. For example, in the case of ZnO, intrinsic defects have been suggested to be the source of the difficulty in achieving a p-doped material [31]. The difficulty arises from an asymmetry between acceptor and donor defects in terms of formation energy that is independent of the chemical potential [31]. It was shown that hole killers such as V_O are abundant while electron killers are rare, thus achieving n-type doping is easier based on intrinsic compensating defects. There are, however, oxides that can be made to exhibit hole conductivity. These oxides

generally exhibit states that hybridize with the valence band edge [32]. In $CuAlO_2$, the cation valence states (Cu d states) hybridize significantly with the oxygen $2p$ states, effectively inducing a curvature of the valence band and therefore creating a reasonable conduction channel for holes [33].

2.1.1.3 Solid state lighting

Solid state lighting in the form light emitting diodes (LEDs) traces its origin to the work of Losev in the 1930ies [34]. Further research led to the realization of red [35] and green LEDs in mid 1900ies. Development of the blue GaN and InGaN LED in the 1990ies [36] was awarded the Nobel prize in 2014 and paved the way for WLEDs. There are a few different design principles of WLEDs and one of the more common is the phosphor converted white light emitting diode (PCWLED) approach [37, 38].

A PCWLED consists of two main parts, a regular LED and a phosphor. The regular LED emits photons through the phosphor with a fraction of the photons passing through and the remaining ones being absorbed. The absorbed photons are effectively down converted (red-shifted) in energy by the creation of phonons in the phosphor and subsequently emitted at a longer wavelength.

Solid state phosphors consist of a host matrix (oxide, silicate, nitride, phosphate etc.) doped with an activator ion, often from the lanthanide series or the transition metals. The optical transitions occurs on the activator ion and the efficacy of the phosphor depends on the interplay between the activator ion and the host matrix. The positions of the activator ion energy levels that partake in the optical transition are one important aspect, and both the ground state level and the excited state level should be located sufficiently far from the band edges of the host matrix. Furthermore, for the purpose of doping, it is advantageous if the size mismatch between the dopand and the species it substitutes is relatively small.

One particular activator ion/host matrix combination is Ce in oxide hosts where the optical transition occurs between the Ce:$4f$ ground state and the excited Ce:$5d$ state. For Ce-doped yttria and rare earth oxide phosphors it has been shown that the efficacy of the Ce:$4f-5d$ luminescence is mainly governed by the magnitude of the band gap of the oxide host [39]. For host matrices with band gaps below 5.6 eV-6.2 eV, the Ce:$4f-5d$ luminescence was shown to be quenched since the Ce:$5d$ states reside above the conduction band edge [39]. Ce-doped YAG is one of the most widely used solid state phosphors [3, 40]. YAG has stoichiometry $Y_3Al_5O_{12}$ and crystallizes in the garnet structure. The formal charge state of Y in YAG is +3 and the valence electron configuration of Ce is $4f^1 5d^1 6s^2$. The isovalent substitution of Y with Ce leaves the $4f$ electron and depletes the higher lying ($5d$ and $6s$) Ce states. The absorption band is centered at around 450 nm [7] (blue part of the visible spectrum), which is compatible with the emission spectrum of certain compositions of $In_{1-x}Ga_xN$. The emission spectrum of Ce:YAG is centered at around 550 nm[7] (yellow part of the visible spectrum). The blue light from

the $In_{1-x}Ga_xN$ LED and the yellow light from Ce:YAG is then perceived as white light.

2.1.1.4 Thermal quenching

Thermal quenching is the observed decrease in luminescence intensity with increasing temperature. This can be a severe drawback for PCWLEDs since down conversion of the absorbed photon *inevitably* dissipates some of the excitation energy as heat and the heat losses can reduce the efficacy of the LED by 10-30% [37]. This can lead to high temperatures in the phosphor, specially at high operating power, and also color distortions. The thermal quenching temperature is quantified by T_x, where x is the fraction of luminescence intensity relative to the low temperature intensity, and is usually reported for $x = 0.5$.

In principle, all mechanisms that impede radiative recombination at the activator ion can lead to luminescence quenching and several mechanisms can be at work simultaneously. In Fig. 2.2 the main luminescence quenching mechanisms are illustrated. These include *i)* landscape crossover, which is a recombination mechanism that proceeds via (multi)phonon emission, *ii)* thermally activated concentration quenching, where the excitation energy migrates through the crystal until it reaches a killer center, and *iii)* thermal ionization, in which the excited electron undergoes a transition to the conduction band and is subsequently captured at an electron trap.

Due to the technological importance of Ce:YAG, thermal quenching has been widely studied, mainly experimentally, in order to elucidate the microscopic origin [6, 7, 39]. Ce:YAG has a very high thermal quenching temperature for dilute Ce concentrations. For Ce concentrations of 0.033%, the quenching temperature was reported to be above 600 K, while for heavily doping (3.33%) it was reduced to 440 K [7]. Due to the strong dependence of Ce concentration, the thermal quenching mechanism for moderate and highly doped Ce:YAG has been attributed to *thermally activated concentration quenching* [7].

Thermally activated concentration quenching requires the presence of electron traps or killer centers (often attributed to point defects) that can either capture the excited state electron or act as an catalyst for non-radiative recombination. Furthermore, it has also been suggested that in dilute Ce:YAG (0.5%), the main quenching mechanism is *thermal ionization* [6]. The attribution to this mechanism was established by thermoluminescence measurements, which showed the presence of electron traps at 0.86 eV and 1.52 eV below the conduction band. The chemical nature of the electron traps was, however, not clarified in that study.

While both thermally activated concentration quenching and thermal ionization ultimately rely on the presence of defects, their role might differ. As illustrated in Fig. 2.2, the defect might act as an electron trap or as a recombination catalyst. In the former case, the Ce atom has lost an electron and thus cannot host optical transitions whereas in the latter case the electron-hole recombination leaves the Ce atom in its original charge state.
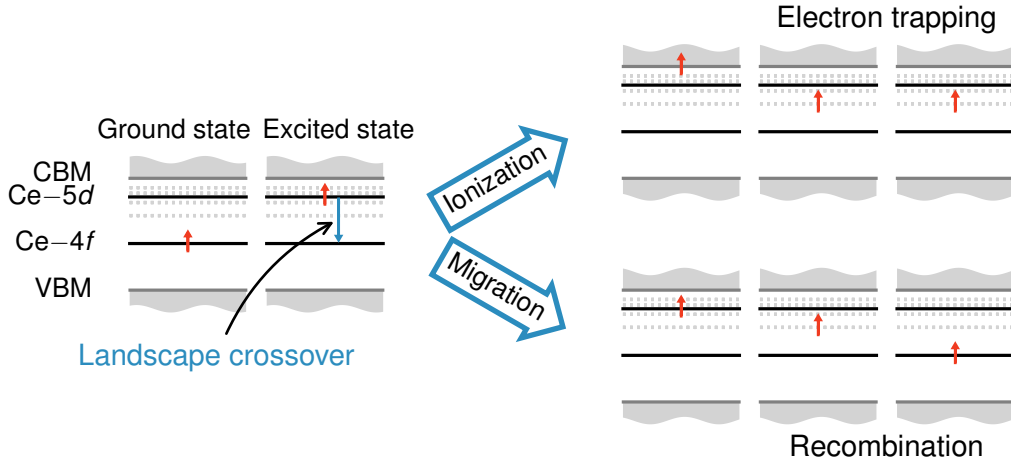
Electron trapping

Ground state Excited state

CBM
Ce−5d
Ce−4f
VBM

Ionization

Migration

Landscape crossover

Recombination

Figure 2.2: Schematic illustration of microscopic mechanisms that would result in luminescence quenching. The dotted gray lines indicate trap levels/killer centers and the blue arrows represent routes the electron (depicted as a red arrow) can take towards luminescence quenching.

2.1.2 Carbides and nitrides

Carbon and nitrogen based compounds with wide band gaps have been shown to be able to host defect induced two-level systems where *individual* defects can be optically manipulated and used as single-photon sources. Furthermore, diamond, SiC, and h-BN all consist of light elements with weak spin-orbit coupling. Single photon emission can be measured with the quantum analogue of the photon correlation function $g^{(2)}(\tau) = \langle I(t)I(t+\tau)\rangle/\langle I(t)\rangle^2$, where I is the light intensity [41]. For a single pure two-level system, this correlation function would tend to zero in the limit of zero time lag. The reason for this behavior is that the excited state of the two-level system has to be populated before photon emission and the excited state exhibits a finite lifetime [42] that depends, among other things, on the transition dipole moment, see Eq. (3.19). The vanishing amplitude of the correlation function corresponds to photon antibunching in contrast to photon bunching as $\tau \to 0$ that is expected from a classical light source [43].

Single photon emission has been shown for the NV^{-1} center in diamond [42] and (presumably) for defects in 4H-SiC [44] and h-BN [4]. In the two latter materials, the understanding of the origin that gives rise to the single-photon emission is not as advanced as for the case of the NV^{-1} center in diamond.

The NV center in diamond consists of a nitrogen atom substituting a carbon atom in combination with a neighboring carbon vacancy. The charge state of this defect is either neutral or negative. In the negative charge state (NV^{-1}), the spin state is $S = 1$ and several in-gap states are present that form an optical system. The importance of single photon emitters is predominantly as building blocks in emerging quantum information

technologies. Single photons generated by the NV^{-1} center in diamond nanocrystals have already been used in quantum cryptography [45]. However, the NV^{-1} center has a shelving state, which gives rise to a deviation from single photon emission at higher operating power [46]. Although many properties, including single-photon emission, are well established for the NV center, there are some intrinsic disadvantages with the NV center. For example, the emission lineshape is rather wide, which makes it difficult to create identical photons, and the transition energy is above ~ 1 eV and thus not suitable for telecommunication applications [47]. Therefore, it is important to identify and advance the knowledge of other single-photon sources. Here, SiC and h-BN are two related materials that can host defects that exhibit single-photon emission.

2.1.2.1 SiC

SiC is a polymorphous material with over 100 different polytypes. One of the more common polytypes is 4H-SiC with a band gap of 3.2 eV [48]. The $N_C V_{Si}$ defect in 4H-SiC is structurally analogous to the NV center of diamond with a transition energy of 1.0 eV [49]. The main difference here, apart from the host matrix, is that the vacant species is silicon instead of carbon. In contrast to the NV center, the $N_C V_{Si}$ defect has not been positively confirmed as a single-photon emitter [50]. However, other defects in 4H-SiC have been proposed to exhibit single-photon emission including $C_{Si} V_C$ [51], and more recent studies have shown that there is a single-photon emitter with brightness that exceeds the NV center in diamond [44].

2.1.2.2 h-BN

Boron nitride is isoelectronic to carbon compounds and exists in similar polytypes depending on temperature and pressure. The cubic structure exhibits a similar crystal structure as diamond and the the hexagonal structure (h-BN) is similar to graphite. At ambient conditions the most stable polytype of boron nitride is likely the cubic structure [52], however, the hexagonal form may be kinetically locked in at these conditions since it is not uncommon at ambient conditions. Monolayers of h-BN can be exfoliated and the wide band gap is retained, hence the electronic structure of monolayer h-BN is very different from the one of graphene.

The wide band gap makes h-BN a promising platform for hosting single photon emitters at room temperature. The wide band gap here is important since thermal quenching rates may be enhanced otherwise (see Sect. 2.1.1.4). In particular, the 2D nature of monolayer h-BN offers significant advantages. It is possible to manipulate surfaces with very high precision and insert emission centers [53]. Furthermore, the properties can be adjusted by different substrates, and total internal reflection may be reduced or even absent [2].

There have been numerous reports of emission centers in h-BN that exhibit single-photon emission [4, 54, 55]. In general, emission from point defects consists of a zero phonon line (ZPL), which is the pure electronic transition energy, and phonon sidebands (see Sect. 3.3.2). The ZPLs of emission centers in h-BN are located in mainly two regions, one band in the visual region between red and green (low frequency band) and one in the near ultraviolet region (high frequency band). The emission in the low frequency band has been reported to have ZPLs at discrete values between 1.6 eV to 2.3 eV with similar optical lineshapes [54] suggesting structural similarity between the different emission sources.

2.2   Optical and thermodynamical properties of TMDs

2.2.1   Transition metal dichalcogenides

Transition metal dichalcogenides (TMDs) is a class of compounds that include a transition metal and a chalcogenide with stoichiometry MX_2 where M = (Mo, W, Pt, Pd, Zr, Hf, ...) and X = (S, Se, Te). These compounds commonly crystallize in hexagonal (H), trigonal (T) or monoclinic (T') layered structures (Fig. 2.3 for monolayer side view), but structures with other symmetries exists as well [56]. The interlayer coupling is due to van-der-Waals (vdW) interactions, while the in-plane bonds are strong with mixed covalento-ionic character. The H type monolayer has mirror plane symmetry, which the T' and T monolayers lack. The commonality of these structures (H, T, and T') among TMD monolayers is shown in Fig. 2.4.

H   T'   T
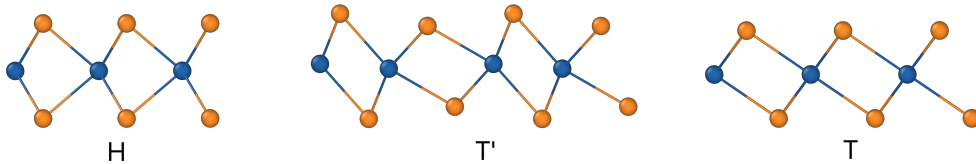
Figure 2.3: Structures of the hexagonal (H), monoclinic (T'), and trigonal (T) transition metal dichalcogenides. The atomic structures were visualized with OVITO [57].

2.2.1.1 MX_2 with M = Mo, W; X = S, Se, Te

The widely studied TMDs MX_2 with M = (Mo, W) and X = (S, Se) crystallize in the H structure [60]. $MoTe_2$ also exhibits H symmetry whereas for WTe_2, the H structure is metastable and the T' structure is the most stable polytype. In bulk form, these are semiconducting vdW solids with indirect band gaps of around 1 to 2 eV [12, 61]. Individual TMD monolayers can be obtained by mechanical exfoliation [62] and perhaps more importantly by chemical vapor deposition [63].

H																	He
Li	Be											B	C	N	O	F	Ne
Na	Mg											Al	Si	P	S	Cl	Ar
K	Ca	Sc	Ti	V	Cr	Mn	Fe	Co	Ni	Cu	Zn	Ga	Ge	As	Se	Br	Kr
Rb	Sr	Y	Zr	Nb	Mo	Tc	Ru	Rh	Pd	Ag	Cd	In	Sn	Sb	Te	I	Xe
Cs	Ba	Lu	Hf	Ta	W	Re	Os	Ir	Pt	Au	Hg	Tl	Pb	Bi	Po	At	Rn

Legend: ■ H ■ T' ■ T

Figure 2.4: Schematic indicating the structures (restricted to H, T, and T') proposed for different TMD monolayers. Data based on Computational 2D Materials Database (C2DB) [58, 59], filtered for systems with stoichiometry MX_2 and high stability. A colored entry should be read as *there is at least one TMD based on this transition metal with this structure*.

The electronic structure of these TMDs depends strongly on the number of layers of the material. In the bulk and bilayer form there is a strong hybridization of valence band zone center and conduction band states at the point halfway between the zone center and K (Fig. 2.5). This valley is referred to as the Λ valley. As the number of layers becomes smaller the electronic structure undergoes a transition from an indirect band gap to a direct band gap (Fig. 2.5 for the band evolution of MoS_2). In the monolayer limit, the valence band and conduction band edges are predominantly composed of transition metal d states (Fig. 2.5).

Since the lattice parameter is almost completely determined by the chalcogen species [58, 61, 64], heterostructures based on the same chalcogen species exhibit vanishing lattice mismatch. The TMDs based on the same chalcogen species exhibit type II band alignment [65] (Fig. 2.1b). For a heterostructure, type II band alignment entails that it is possible to obtain a spatial separation between the valence band and conduction band since these reside in different parts of the material. In the case of vertical heterostructures, the type II alignment may lead to excitations where the electron resides in one layer and the hole in the other.

2.2.2 Excitons

For TMDs, the optical spectra are dominated by excitons [67]. An exciton is a bound electron hole pair. Due to the Coulomb interaction in a material, the electron and hole exhibit an attractive interaction that correlates the motion of the electron and of the hole. The exciton is characterized by a binding energy, which can be understood as the difference between the quasi-particle band gap energy and the exciton energy. The binding
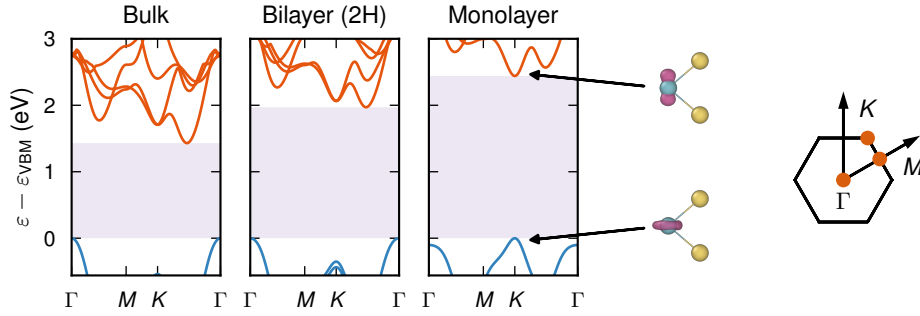
Figure 2.5: The PBE band structure of bulk, bilayer, and monolayer MoS_2 with the band gaps shifted to the GLLB-SC [66] band gaps. The conduction band edge in the bulk and bilayer occurs at the Λ point, i.e., half way between the zone center and the K-point. Spin-orbit coupling has not been accounted for.

energy is indicative of the energy required to break up the correlated electron hole pair to form a free electron and a free hole. The exciton is typically the lowest electronic interband optical excitation and in, e.g., bulk GaN, the exciton binding energy is estimated to be around 20 meV [68], and thus not stable at room temperature, while in hafnia it has been predicted to be around 570 meV [69].

One of the reasons that the exciton binding energy varies so much between materials is that it is strongly dependent on the dielectric screening. In 2D materials, due to the dimensionality reduction the Coulomb interaction is stronger and the dielectric screening is weaker compared with bulk materials [16, 70]. It was estimated in another theoretical study that the monolayer MoS_2 exciton binding energy was 40 times larger than the bulk exciton binding energy [70]. The ground state (1s) exciton binding energy has been shown to be well approximated within certain limits by the following general form in 2D materials [16]

$$E = \frac{8\mu}{\left(1 + \sqrt{1 + \frac{32\pi\alpha\mu}{3}}\right)^2},$$ (2.1)

where μ is the exciton effective mass and α is the 2D polarizability.

In order to model excitons it is necessary to describe the screened Coulomb interaction between carriers (electrons and holes), which is a computationally demanding task. The Bethe-Salpeter equation is a first-principles method to compute the optical spectra, which includes excitonic effects. In the studies connected to this thesis (**Paper V** and **Paper VI**), however, the exciton properties has been computed using density matrix theory with certain parameters estimated from DFT calculations.

2.2.3 Bilayers and moiré superlattices

The main purpose of this section is to introduce twisted (moiré) bilayers, but first the properties of untwisted 2D bilayers are addressed.

Monolayers can be stacked to form bilayers, with the stacking order determining much of the properties of the bilayer. A hexagonal system with a basis consisting of atoms A and B can be stacked in AA or AB order. There is also an additional number of stacking orders arising from a relative translation of monolayer in these two fundamental stacking orders. There are several ways to refer to specific stacking orders and one commonly used is based on $R^X_{X'}$ ($H^X_{X'}$), where R (H) refers to the AA (AB) parent stacking while the superscript X and subscript X' indicate the sites that are vertically aligned (Fig. 2.6). For example, R^h_h is the bilayer stacking with parent stacking AA and where the midpoints of the hexagon (denoted h for hollow) are vertically aligned. This is just parent stacking AA, while R^A_h would mean that the parent stacking AA is subject to a relative translation such that the atom A of the top layer is vertically aligned to the hexagonal midpoint of the bottom layer. This bilayer stacking is also referred to as Bernal stacking.
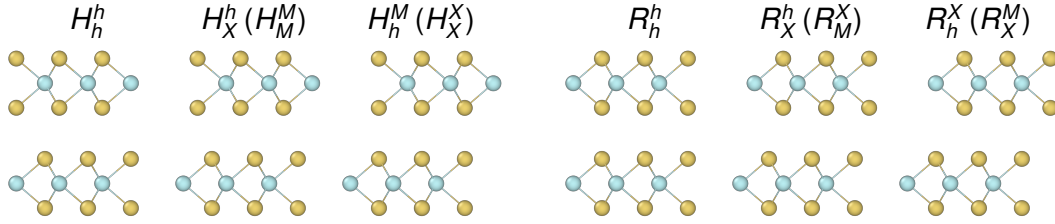
Figure 2.6: Side view of atomic registries using a $2 \times 2 \times 1$ supercell for different stacking orders with M atoms in blue and X atoms in yellow. The atomic structures were visualized with OVITO [57].

A general feature of bilayer formation in TMDs is the strong hybridization that occurs between the layers, in particular between the valence band zone center states and the conduction band Λ states. This has the effect that the zone center valence band is pushed to larger energies rendering the band gap indirect. The magnitude of the hybridization is stacking dependent. The binding energy and interlayer distance are greatly affected by the stacking order, see Fig. 2.7 for predictions based on conventional DFT calculations using the vdW-df-cx exchange correlation functional [71]. The AB fundamental stacking is the most stable stacking order for bilayer MoS_2 according to calculations using the vdW-df-cx functional ($\approx 1\,\mathrm{meV}$ below R^h_X), there are situations in which other stacking orders will be present.

The bilayer system has additional degrees of freedom, e.g., a relative rotation. A small relative rotation of one monolayer with respect to the other can result in a structure that exhibits an interference pattern in the atomic positions, which is also called a moiré pat-

Figure 2.7: Total energy of the MoS_2/MoS_2 bilayer in different stacking orders with respect to the minimum energy of the H_h^h stacked structure computed in connection to the study in **Paper VII** using the vdW-df-cx functional.

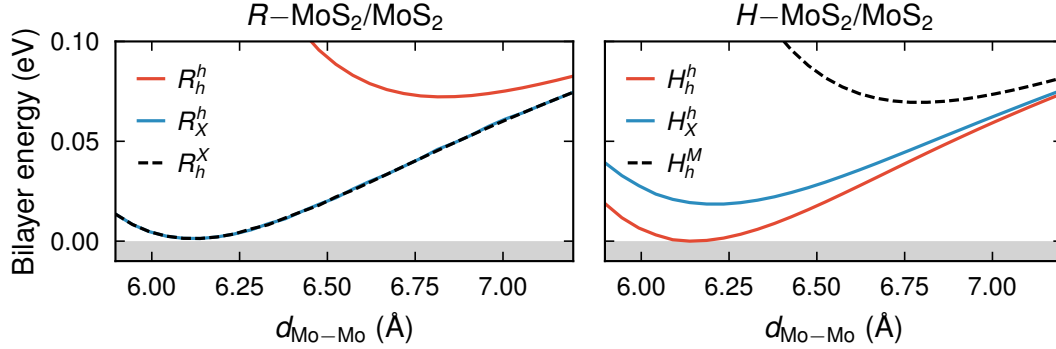tern. These structures can exhibit properties that are vastly different from the untwisted bilayers. Non-dispersive states have been shown to emerge in twisted graphene [72], h-BN [73], and TMDs [74]. The emergent flat bands can give rise to strongly correlated phenomena such as superconductivity and the most famous example of a twist induced phenomenon is probably the emergence of superconductivity at a twist angle of 1.1° in twisted graphene [72].

In a moiré structure there is an alternating stacking order throughout the system (Fig. 2.8) and two additional positions in the moiré structure where there is a local C_3 symmetry with stacking corresponding to a relative translation of 1/3 and 2/3 (in units of the long diagonal) of one monolayer along the long diagonal of the bilayer unit cell. These two positions exhibit the stacking order shown in Fig. 2.6, where the stacking orders are separated by domain walls (Fig. 2.8).

2.2.3.1 Derivation of commensurate angles

The construction of a commensurate hexagonal moiré supercell is a purely geometrical problem [75–77]. The derivation is based on the criterion that translations of the lattice points in the untwisted and twisted layer must coincide somewhere.

The derivation follows the approach of Ref. [75] and the main obstacle is solving a non-linear homogeneous Diophantine equation. The unit cell lattice vectors for a hexagonal 2D system are $\mathbf{a}_1 = a_0(1,0)$ and $\mathbf{a}_2 = a_0(-\frac{1}{2}, \frac{\sqrt{3}}{2})$, where a_0 is the lattice constant. The position of lattice point (i, j) is

$$\mathbf{P}_{ij} = i\mathbf{a}_1 + j\mathbf{a}_2 = a_0 \begin{pmatrix} i - \frac{1}{2}j \\ j\frac{\sqrt{3}}{2} \end{pmatrix} = a_0 \begin{pmatrix} 1 & -\frac{1}{2} \\ 0 & \frac{\sqrt{3}}{2} \end{pmatrix} \begin{pmatrix} i \\ j \end{pmatrix}. \tag{2.2}$$

Figure 2.8: *H* and *R* stacked moiré superlattices at a twist angle of 4.41° with the high-symmetry positions indicated. The atomic structures were visualized using the software OVITO [57].

The twisted monolayer has basis positions (i', j') at the following positions

$$\mathbf{P}'_{i'j'} = \mathbf{R}_\theta[i'\mathbf{a}_1 + j'\mathbf{a}_2] = a_0 \begin{pmatrix} \cos\theta & -\frac{1}{2}\cos\theta - \frac{\sqrt{3}}{2}\sin\theta \\ \sin\theta & -\frac{1}{2}\sin\theta + \frac{\sqrt{3}}{2}\cos\theta \end{pmatrix} \begin{pmatrix} i' \\ j' \end{pmatrix}. \tag{2.3}$$
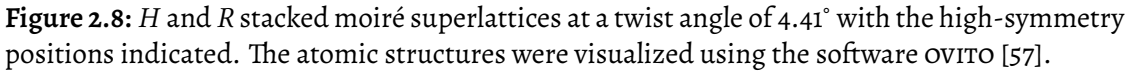
For a commensurate twist angle $\mathbf{P}_{ij}$ and $\mathbf{P}'_{i'j'}$ must coincide for some point(s) in order to maintain periodicity, therefore non-trivial solutions to $\mathbf{P}_{ij} = \mathbf{P}'_{i'j'}$ with the unknowns i, j, i', and j' are required. The inverse of the translation matrix is

$$a_0 \begin{pmatrix} 1 & -\frac{1}{2} \\ 0 & \frac{\sqrt{3}}{2} \end{pmatrix}^{-1} = \frac{2}{a_0\sqrt{3}} \begin{pmatrix} \frac{\sqrt{3}}{2} & \frac{1}{2} \\ 0 & 1 \end{pmatrix} \tag{2.4}$$

and the equation becomes

$$\mathbf{P}_{ij} = \mathbf{P}'_{i'j'} \implies \begin{pmatrix} i \\ j \end{pmatrix} = \begin{pmatrix} \cos\theta + \frac{1}{\sqrt{3}}\sin\theta & -\frac{2}{\sqrt{3}}\sin\theta \\ \frac{2}{\sqrt{3}}\sin\theta & \cos\theta - \frac{1}{\sqrt{3}}\sin\theta \end{pmatrix} \begin{pmatrix} i' \\ j' \end{pmatrix} = \mathbf{M} \begin{pmatrix} i' \\ j' \end{pmatrix}. \tag{2.5}$$

From the elements of $\mathbf{M}$ it is clear that only specific values of θ will make $\mathbf{M}$ rational valued. We follow the approach of Ref. [75] and set $\alpha = \cos\theta$ and $\beta = 3^{-1/2}\sin\theta$ and

$$\begin{pmatrix} i \\ j \end{pmatrix} = \begin{pmatrix} \alpha + \beta & -2\beta \\ 2\beta & \alpha - \beta \end{pmatrix} \begin{pmatrix} i' \\ j' \end{pmatrix}, \tag{2.6}$$

with $\alpha, \beta \in \mathbb{Q}$. Since the matrix $\mathbf{M}$ is an area preserving map, the determinant is 1 and we get the constituent relation of α and β as

$$\alpha^2 + 3\beta^2 = 1, \tag{2.7}$$

which is the Diophantine equation $A^2 + 3B^2 = C^2$, with $\alpha = A/C, \beta = B/C$. This equation can be solved by looking for rational points on an ellipse (similar to finding rational points on the unit circle in order to solve for Pythagorean triplets). The solution can be parameterized as

$$\beta = u \quad \text{and} \quad \alpha = -\frac{P}{Q}u + 1, \quad P, Q \in \mathbb{Z}^+.$$

Insertion of the parameterized solution in Eq. Eq. 2.7 yields

$$u = \frac{2PQ}{3Q^2 + P^2}. \tag{2.8}$$

This gives

$$\mathbf{M} = \frac{1}{3Q^2 + P^2} \begin{pmatrix} 3Q^2 - P^2 + 2PQ & -4PQ \\ 4PQ & 3Q^2 - P^2 - 2PQ \end{pmatrix}. \tag{2.9}$$

The commensurate twist angles are then (by substituting M_{21} or M_{12}) given by

$$\sin(\theta_{PQ}) = \frac{8\sqrt{3}PQ}{3Q^2 + P^2}. \tag{2.10}$$

By choosing $P = 1$ and $Q = 2k + 1$, one obtains the expression for the twist angles [77] that was used in **Paper VII**, as was noted in Ref. [75] albeit with a different expression. The expression here is

$$\theta_k = \arcsin\left(\frac{\sqrt{3}}{2}\left[\frac{2k+1}{3k^2 + 3k + 1}\right]\right). \tag{2.11}$$

For this choice of P and Q, the twist angles that results in commensurate moiré super-lattices exhibit a rather large angle spacing for twist angles larger than 5°. However, for low twist angles the angle spacing becomes much smaller.

2.2.4 Binary alloys

In this section, the thermodynamics of TMD alloys is outlined. TMDs is a class of materials with stoichiometry MX_2, where M is a transition metal and X is a chalcogen. These (presumably) do not substitute easily with each other and therefore it is possible to have substitutional alloys on either one of the M sublattice or X sublattice. For alloys with mixing on the M sublattice, there could in principle be mixing of transition metals from different groups of the periodic table.

For TMD alloys, one can distinguish between three different types of mixing behavior at 0 K. These are *i)* ordered mixing systems, *ii)* non-mixing systems, and *iii)* Janus

systems. The Janus phase is only possible for alloys with mixing on the X site and consists at $x = 0.5$ of a structure with chalcogen layers with different species. The mixing behavior is determined by the free energy.

A binary substitutional alloy exhibits mixing of two elements on one sublattice. For the case of a TMD that exhibits stoichiometry MX_2 with mixing on the M site, the mixing energy is

$$\Delta E_{\text{mix}}(x) = E(M_n M'_m X_{2(n+m)}) - nE(MX_2) - mE(M'X_2), \tag{2.12}$$

where $x = n/(n + m)$. Disregarding the changes in vibrational entropy, the mixing free energy is

$$\Delta G_{\text{mix}}(x) = \Delta E_{\text{mix}}(x) - T\Delta S_{\text{conf}}(x). \tag{2.13}$$

The configurational entropy of a random solution can be approximated by a mean field model as [78]

$$\Delta S_{\text{conf}}(x) = -k[x \ln x + (1 - x)\ln(1 - x)]. \tag{2.14}$$

More accurate predictions of the mixing entropy can be realized by sampling via Monte Carlo simulations using a suitable lattice model such as an alloy cluster expansion [79].

Now Eq. 2.13 is only valid in the case of a homogeneous concentration throughout the alloy, something that may not be the case. If the sample consist of two regions with concentrations x_1 and x_2 such that the average concentration is $\bar{x} = \gamma x_1 + (1 - \gamma)x_2$, the free energy is

$$\Delta G_{\text{mix}}(\bar{x}) = \gamma \Delta G_{\text{mix}}(x_1) + (1 - \gamma)\Delta G_{\text{mix}}(x_2), \tag{2.15}$$

where γ can be expressed in the concentrations as

$$\gamma = \frac{\bar{x} - x_1}{x_1 - x_2}. \tag{2.16}$$

For each temperature, the common tangent of two minima of $\Delta G_{\text{mix}}(x)$ can be used to assess the range of concentrations for which mixing does not occur. If the tangent falls below $\Delta G_{\text{mix}}(x)$ the system can attain a lower free energy by phase separation.

In order to predict a quantity Q as a function of composition, e.g., the lattice parameter, band edge positions, or band gap, the following expression is often used

$$Q(x) = x\,Q(x = 0) + (1 - x)\,Q(x = 1) - b\,x\,(1 - x), \tag{2.17}$$

where b is the bowing parameter. If the bowing parameter can be neglected the resulting expression is referred to as Vegard's law.

3

Point defects

There are different notation schemes for defects. The convention adopted throughout this thesis is A_B^q, where A is the defect and B is the site and q indicates the charge state. In the case of a substitutional defect, A is the chemical symbol of the introduced atom and B is the chemical symbol of the atom that is replaced. For a vacancy, the defect is denoted by V and for an interstitial the site is labeled with I. The charge state is with respect to the atom and not the ion, e.g., a vacant O^{2-} is denoted by V_O^{+2}. This notation differs from the Kröger-Vink notation (used in **Paper II**) where positive charges are labeled with •, negative charges with ′ and neutral defects with ×. For example V_O^{+2} is denoted as $V_O^{\bullet\bullet}$ in Kröger-Vink notation. Zero-dimensional defects that cannot be described within this notation are, e.g., topological defects such as Stone-Walls defects, which causes the atomistic connectivity to change and the notion of sites becomes ambiguous.
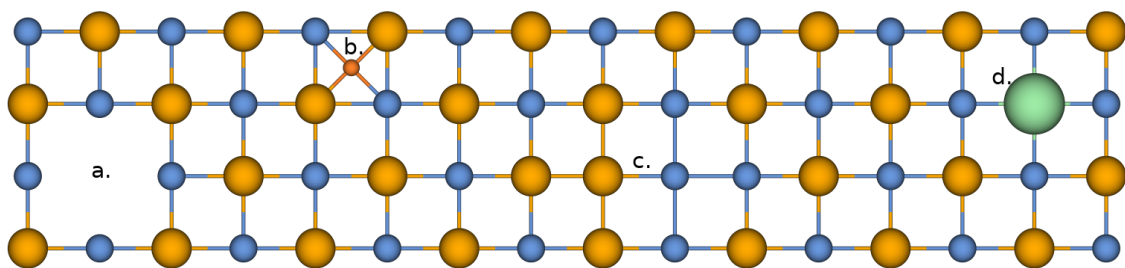
Figure 3.1: Illustration of point defects including (a) vacancy defect, (b) interstitial, (c) double anti site defect, and (d) substitutional defect.

A few types of point defects are illustrated in Fig. 3.1. In addition to the point defects that affect a single site such as vacancies, interstitial and substitutional defects, there are more complex defects such as vacancy-substitutional complexes that are composed of several point defects. Vacancies, interstitials, and substitutional atoms are likely to

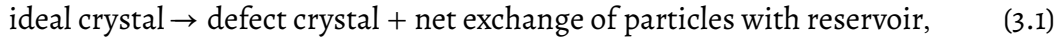be more common (since these are constituents of more complex defects) than more complex defects but the overall prevalence in equilibrium is mainly governed by the formation energy of the defect, which depends on the environment of the crystal.

3.1 Thermodynamics

The formation energy is the most central quantity associated with a defect since it governs the *equilibrium* concentration of said defect. It is a measure of the energy cost to create the defect. The formation energy provides a means to analyze charge state stability regions and can be used to quantify transition energies.

3.1.1 Formation energy

The formation of a defect is analogous to a chemical reaction in which several reactants form a final product. As such the change in Gibbs free energy $\Delta G = \Delta H - T\Delta S$ governs the formation of defects. A general reaction for the formation of a defect can be expressed as

$$\text{ideal crystal} \rightarrow \text{defect crystal} + \text{net exchange of particles with reservoir,} \qquad (3.1)$$

where the particles are both ions and electrons. The internal energy difference for a single defect in charge state q is then

$$\Delta E = E^q_{\text{defect}} - E_{\text{ideal}} - \sum_i \mu_i \Delta N_i, \qquad (3.2)$$

where ΔN_i is referenced to the ideal crystal, e.g., $\Delta N = -1$ for a vacancy.

The total enthalpy difference in the case of formation of n non-interacting identical defects in charge state q is

$$\Delta H = n[E^q_{\text{defect}} - E_{\text{ideal}} - \sum_i \mu_i \Delta N_i] + p\Delta V, \qquad (3.3)$$

where ΔV is the change in volume by the incorporation of n defects. The entropy increase originates from vibrational and configurational contributions. If the defect concentration is low enough, the defect induced difference in the vibrational degrees of freedom is independent of other defects. The changes of the vibrational entropy is then a local quantity associated with a defect while the configurational entropy is a global quantity, i.e., $\Delta S = n\Delta S_{\text{vib}} + \Delta S_{\text{conf}}$. The change in Gibbs free energy is then

$$\Delta G = n[E^q_{\text{defect}} - E_{\text{ideal}} - \sum_i \mu_i \Delta N_i - T\Delta S_{\text{vib}}] + p\Delta V - T\Delta S_{\text{conf}}. \qquad (3.4)$$

In an insulator the chemical potential of the electron is usually positioned within the band gap but can also be located within the band manifolds in the case of degenerately doped semiconductors at low temperatures. The electron chemical potential is μ_e. The dominating quantity of ΔH is the *formation energy*, which for a defect in charge state q is defined as [80]

$$\Delta E_F = E^q_{\text{defect}} - E_{\text{ideal}} - \sum_i \mu_i \Delta N_i + q(\varepsilon_{\text{VBM}} + \delta\mu_e), \tag{3.5}$$

where i runs over ions only. At equilibrium ΔS_{conf} balances the number of defects so that $\Delta G = 0$. A positive formation energy indicates that the ideal crystal is thermodynamically stable with respect to formation of the specific defect at 0 K. The Gibbs free energy ΔG is then

$$\Delta G = n[\Delta E_F - T\Delta S] + p\Delta V - T\Delta S_{\text{conf}}. \tag{3.6}$$

3.1.2 Configurational entropy

The configurational entropy in Eq. 3.4 for a system with n identical non-interacting defects distributed over N available lattice sites can be expressed as $\Delta S_{\text{conf}} = k_B \log W$ with $W = \dfrac{N!}{n!(N-n)!}$. The change in entropy is then found by using Stirling's approximation as both n and N are very large. The result is

$$\Delta S_{\text{conf}} = k_B \left[N \log\left(1 - \frac{n}{N}\right) - n \log\left(\frac{N}{n} - 1\right) \right]. \tag{3.7}$$

The change in configurational entropy with respect to the number of defects is

$$\frac{d\Delta S_{\text{conf}}}{dn} = k_B \log\left(\frac{N}{n} - 1\right). \tag{3.8}$$

The entropy difference tends to $+\infty$ as N/n tends to $+\infty$, which means that the entropy of the system increases spectacularly by the formation of defects and at any finite temperature it is very difficult to fabricate defect-free materials. The equilibrium concentration of defects can be found from

$$\frac{d\Delta G}{dn} = 0 \Leftrightarrow \frac{n}{n+N} = \exp\left(-\frac{\Delta E_F}{k_B T}\right) \exp\left(\frac{\Delta S_{\text{vib}}}{k_B}\right) \exp\left(-\frac{p}{k_B T}\frac{d\Delta V}{dn}\right). \tag{3.9}$$

If $N \gg n$ and the vibrational entropy and change in volume are small (≈ 0) the equilibrium defect concentration is

$$\frac{n}{N} \approx \exp\left(-\frac{\Delta E_F}{k_B T}\right). \tag{3.10}$$
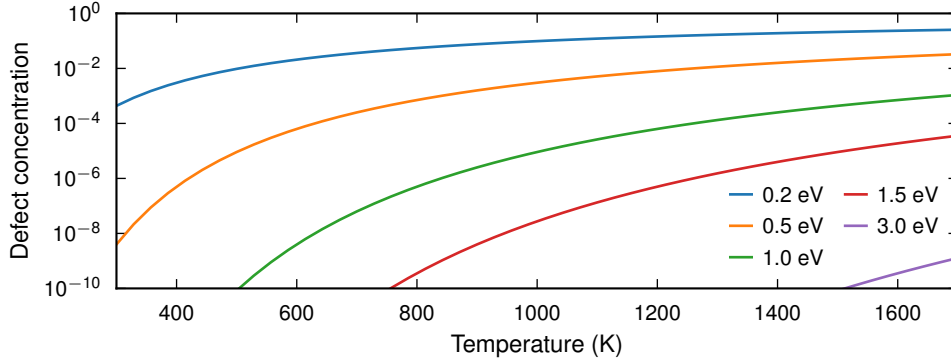
25

Figure 3.2: Equilibrium concentration of defects as a function of temperature for a set of different formation energies.

The defect concentration for a range of different formation energies is shown in Fig. 3.2. For example, for a defect formation energy of 0.5 eV at 600 K one can expect that around one in ten thousand sites to be a defect in equilibrium.

For very large defect concentrations the defects may not be evenly/randomly distributed in the material. In the cases of high oxygen vacancy concentration in some wide band oxides, the vacancies tend to aggregate and form so-called Magnéli phases instead where the vacancies are located in a shear plane [81].

3.1.3 Charge transition levels

The formation energy can be used to assess the charge state stability regions with respect to the electron chemical potential. Equating ΔE_F (Eq. 3.5) for a defect in two different charge states q_1 and q_2 results in

$$\delta\mu_e = \frac{E_{\text{defect}}^{q_1} - E_{\text{defect}}^{q_2}}{q_2 - q_1} - \varepsilon_{\text{VBM}}.$$

(3.11)

The equilibrium formation energy as a function of electron chemical potential can exhibit a kink at the relative electron chemical potential on the left hand side of Eq. 3.11. This kink indicates the charge transition level (CTL) between charge states q_2 and q_1. The position of the CTL with respect to the band edges is an important characteristic of a defect since it determines much of the influence the defect has on the electronic and optical properties of the system.

3.1.4 Chemical potential

The chemical potentials of the atomic species that occurs in, e.g. Eq. 3.5 are subject to several constraints. The chemical potential of species i is limited from above by the elemental phase [82]

$$\mu_i \leq \mu_i^0. \tag{3.12}$$

For a monoatomic crystal, the only phase boundary is the elemental solid/molecule. For compound crystals, the equilibrium stability of the crystal couples the chemical potentials of the constituent species and therefore additional constraints are imposed depending on the stoichiometry of the compound. In binary compounds with stoichiometry of AB the chemical potentials are coupled as [82]

$$\mu_{AB} = \mu_A + \mu_B. \tag{3.13}$$

Using the upper bound (Eq. 3.12) of μ_A and μ_B one finds the range of chemical potentials for A and B as

$$\mu_{AB} - \mu_B^0 < \mu_A < \mu_A^0 \tag{3.14}$$

$$\mu_{AB} - \mu_A^0 < \mu_B < \mu_B^0. \tag{3.15}$$

The limit where $\mu_A \rightarrow \mu_A^0$ is called the A-rich limit and $\mu_A \rightarrow \mu_{AB} - \mu_B^0$ is called the A-poor limit and similarly for B. The elemental chemical potentials of A and B are related to μ_{AB} and the formation enthalpy $\Delta H_f(AB)$ as [80]

$$\Delta H_f(AB) = \mu_{AB} - \mu_A^0 - \mu_B^0, \tag{3.16}$$

which makes it impossible to choose both μ_A and μ_B as the elemental phases, i.e., there cannot be both an A-rich and a B-rich environment simultaneously.

For a gas phase reservoir the chemical potential depends on pressure and temperature of the gas. For a gas phase dimer such as O_2 the chemical potential is [80]

$$\mu_O = \mu_O^0 + \frac{k_B T}{2} \left(\log \left[\frac{PV}{k_B T} \right] - \log[Z_{rot}] - \log[Z_{vib}] \right), \tag{3.17}$$

where $V = [h^2/(2\pi m k_B T)]^{3/2}$ and Z is the partition function.

3.1.5 Electron chemical potential

The formation energy of a charged defect is linearly dependent on the electron chemical potential μ_e. However, the electron chemical potential is in turn dependent on the formation energy via the connection between defect concentration and formation energy (in the case of n identical non-interacting defects see Eq. 3.10).

In *equilibrium* μ_e is determined by charge neutrality conditions where the charge states of several different types of defects balance the free electron and hole concentrations. The free charge carrier concentration is a result of ionized defects. In principle, one could fully self-consistently solve for the μ_e if the formation energy of all defects in the relevant charge states are known. However, for large defect concentrations Eq. 3.10 may not be a satisfactorily relation between formation energy and concentration and the configurational entropy may need to be sampled through, e.g., Monte Carlo simulations.

3.2   Electronic structure

A defect in a band gap material can exhibit multiple thermodynamically stable charge states, where the equilibrium charge state is determined by the electron chemical potential. This is a fundamentally important concept that underpins much, if not all of semiconductor industry and is important in insulators as well since it is related to fundamental material properties such as the doping ability.

The fact that that defects can exhibit different stable charge states can be utilized to increase the electrical conductivity of a band gap material by doping with suitable dopants. The position of the $(n + 1/n)$ CTL for electron donor defects and the $(n - 1/n)$ CTL for electron acceptor defects determine how easily a defect can be ionized. A shallow defect state is a defect state for which the $(n + 1/n)$ CTL ($(n - 1/n)$ CTL) is located sufficiently close to the conduction (valence) band edge, whereas a deep defect state exhibits a CTL that is located deeper in the band gap. In Fig. 3.3a, the formation energy diagram for the nitrogen vacancy in AlN is shown. There are several CTLs that correspond to deep defect states. Deep defects in principle cannot donate or accept electrons from the band edges at moderate temperatures via thermal ionization. Deep defect states are *usually* confined to an environment in the close proximity of the defect.

Furthermore, due to the confinement of the single particle wave function for a deep defect state, the local geometry may differ significantly between different charge states of the defect due to charge localization. This is rather defect specific, for example the C_N defect in monolayer h-BN exhibits only a minor local geometry variation upon a charge state transition whereas the oxygen vacancy in MgO exhibits a large local geometry difference between the stable charge states. The local geometry distortion upon charge state change may be more prominent for anion vacancies in ionic solids due to the free volume associated with the vacancy in combination with the localization of charge compared with charge state transitions on substitutional defects.

Transitions that involve defect states may be of two different types that require different modeling approaches. The different transitions are schematically illustrated in Fig. 3.3b. The first transition is the transition where one of the states is a band state. This is a charged transition and is modeled using formation energies of charged defects (Sect. 3.1.1). The second type of transition is a charge neutral transition where an elec-
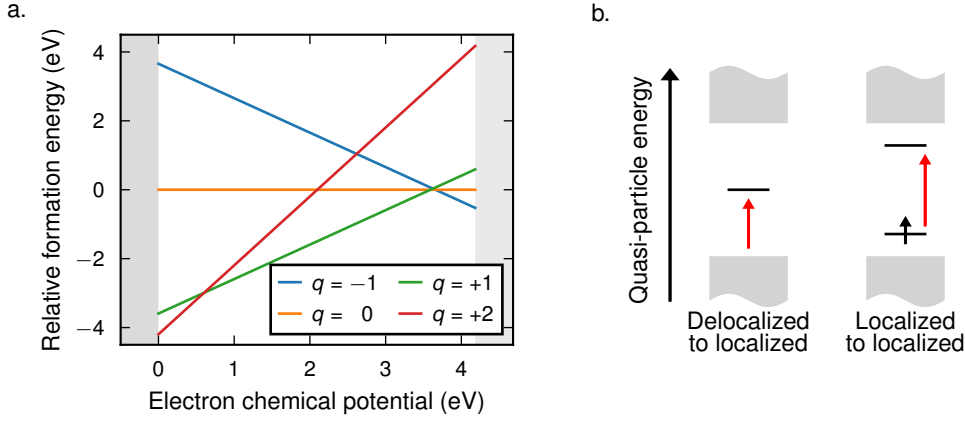
Figure 3.3: a) Illustration of the appearance of deep defect states in a formation energy diagram. The present case is for the nitrogen vacancy in hexagonal AlN computed with PBEsol [83], a 4×4×3 supercell and omission of image charge corrections. b) Schematic illustration of two different transitions (red arrows) involving defect states. In one transition, a valence band state is excited to the empty in-gap defect state. In the other transition a defect bound electron is excited to an empty in-gap defect state.

tron bound to the defect is excited to an empty defect state and the modeling of this transition is also performed using total energy differences. The energy of the excited state can be computed using the ΔSCF method (Sect. 4.2.6).

3.3 Optical properties

Electronic transitions involving defects can be divided into two major types of transitions. These are interband and intraband transitions. Examples of intraband transition are the scattering of hot electrons and holes on defects. This section is concerned with interband transitions, which are either coupled to photons and phonons.

3.3.1 Radiative transitions

Radiative transitions can be further divided into different types, depending on the character of the involved electronic states (Fig. 3.3). The localized to delocalized transition involves a band edge state as the initial or final state, which is delocalized while the localized-localized transition involves two localized defect states. Another type of transition is the donor-acceptor pair transition, which involves defect states from different defects. The possibility of a radiative transition is dependent on a non-zero transition dipole moment between the initial and final state. The donor acceptor pair transition is unlikely in the case of very deep acceptor and donors unless the donor and acceptor are

located in close vicinity of each other due to the confinement of the defect state wave functions. The rate of absorption and spontaneous emission are given by the Einstein B and A coefficients. For the case of spontaneous emission, the number of emitted photons is proportional to the number of excited electrons n, i.e.,

$$\frac{dn}{dt} = -A\,n \longrightarrow n = e^{-At}. \tag{3.18}$$

The quantity A is the radiative transition rate and it is called the Einstein A coefficient. The Einstein A coefficient can be expressed as [84]

$$A = \frac{e^2 \omega_{\mathrm{ZPL}}^3 |\mu|^2}{3\pi\varepsilon_0 \hbar c^3}, \tag{3.19}$$

where μ is the transition dipole moment. The transition dipole moment is defined as

$$\mu_{ij}(\mathbf{R}) = \int d\mathbf{r}\, \mathbf{r}\psi_i(\mathbf{r}, \mathbf{R})^\dagger \psi_j(\mathbf{r}, \mathbf{R}), \tag{3.20}$$

where $\mathbf{R}$ denotes the set of ionic coordinates.

3.3.2 Vibronic transitions involving defect states

Radiative vibronic transitions are transitions that involve both a vibrational transition and an electronic transition, i.e.,

$$\varepsilon_i + \sum_i n_i \hbar \left(\omega_i + \frac{1}{2} \right) \to \varepsilon_j + \sum_j n_j \hbar \left(\omega_j + \frac{1}{2} \right). \tag{3.21}$$

Fig. 3.4 shows the potential energy landscapes of the initial and final states that partake in the transition for the case of a single vibrational degree of freedom. In this regard, transitions involving the creation of 0, 1, and 2 phonons are indicated. The governing equation for the optical lineshape is Fermi's golden rule

$$I(\omega) = C\omega^k \sum_f \langle \Psi_i | \mu | \Psi_f \rangle \delta(E_f - E_i \pm \omega), \tag{3.22}$$

where C is a constant and $k = 1$ for absorption and $k = 3$ for emission [85]. Ψ are wave functions: $\Psi = \psi\chi$. Here, ψ is the electronic component and χ is the vibrational component.

3.3.2.1 Franck-Condon approximation

From Eq. 3.20 and Eq. 3.22, the transition dipole moment carries a dependence on the ionic coordinates and it is difficult to account for this dependence. The first order series expansion is

$$\mu_{ij}(\mathbf{R}) \approx \mu_{ij}(\mathbf{R}_0) + \frac{1}{2} \sum \nabla \mu_{ij}(\mathbf{R})\big|_{\mathbf{R}_0} \cdot (\mathbf{R} - \mathbf{R}_0). \tag{3.23}$$

Keeping *only* the constant term corresponds to the Franck-Condon approximation [86]. In this approximation the transition dipole moment can be factored out so that $I(\omega) \propto \omega^k F(\omega)$ where F is the lineshape function

$$F(\omega) = \sum_f \langle \chi_i | \chi_f \rangle \, \delta(E_f - E_i \pm \omega). \tag{3.24}$$

The remaining probability distribution depends only on the overlaps of the vibrational wave functions. The relative displacement of the potential energy surfaces (Fig. 3.4) is therefore an early indicator for how likely certain transitions are. Including the first order term in Eq. 3.23 corresponds to the so called Herzberg-Teller approximation [86].

3.3.2.2 Electron phonon spectral function

The vibrational wave function overlaps $\langle \chi_i | \chi_j \rangle$ are difficult to compute so in order to be able to account for the coupling to the vibrational degrees of freedom a set of approximations has to be imposed to arrive at a computationally feasible scheme. First, there is the Franck-Condon approximation and then the additional approximations are *i)* the harmonic approximation, *ii)* the approximation that the vibrational modes of the excited and ground state are the same, usually called the *parallel mode approximation*, and finally *iii)* that the transition occurs at low temperatures. Under these approximation the electron phonon spectral function can be obtained from the (semi-classical) transition energy difference

$$\Delta E(Q) = \Delta E_{\text{ZPL}} + \frac{1}{2} \sum_\nu \omega_\nu^2 [(Q - Q_{\nu,f})^2 - (Q - Q_{\nu,i})^2], \tag{3.25}$$

where Q are normal mode coordinates. The low temperature approximation is such that absorption occurs from $Q = Q_i$ (and analogously, emission would occur from $Q = Q_f$) and the mode decomposed vibrational transition energy is then

$$\Delta E_\nu = \frac{1}{2} \omega_\nu^2 \Delta Q_{\nu,if}^2. \tag{3.26}$$

The strength of the coupling between a transition and phonon mode ν is quantified in the dimensionless *partial* Huang-Rhys (HR) factor s_ν obtained in this case as

$$s_\nu = \frac{\Delta E_\nu}{\hbar \omega_\nu} = \frac{\omega_\nu \Delta Q_{\nu,if}^2}{2\hbar}. \tag{3.27}$$
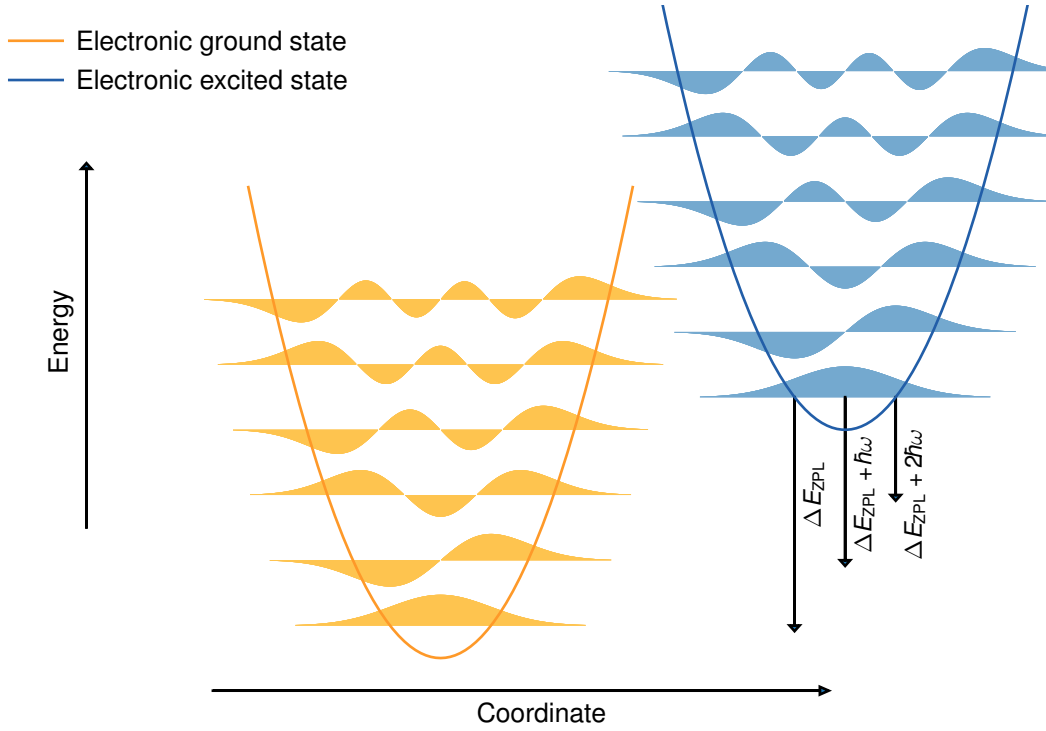
Figure 3.4: The ground and excited electronic state with vibrational levels included illustrated for the case of a single coordinate. Electronic transitions associated with photon and phonon emission are indicated. The indicated transitions occur from the vibrational ground state of the excited electronic state corresponding to the low temperature approximation.

The partial HR factor s_v is the mean number of phonons with frequency ω_v involved in the transition. From the partial HR factors, the electron-phonon spectral function is defined as [9]

$$S(\omega) = \sum_v s_v \delta(\omega - \omega_v). \tag{3.28}$$

Finally, the (total) HR factor is

$$S = \sum_v s_v = \int_0^\infty d\omega\, S(\omega). \tag{3.29}$$

The magnitude of S has a significant influence on the phonon sidebands. It is possible to distinguish between two limiting regimes, weak coupling ($S \lesssim 5$) and strong coupling $S \gtrsim 5$. For the case of a *single* vibrational mode with a HR factor of S, the probability for emission of n phonons at low temperatures follows the Poisson distribution [87]

$$P(n) = \exp(-S)\frac{S^n}{n!}. \tag{3.30}$$

In Fig. 3.5, the distribution is shown for different values of the HR factor. In the strong coupling regime, the phonon sideband becomes wide and the probability of a zero phonon transition vanishes. Here, the probability of a zero phonon transition is just $\exp(-S)$. The center and width of the sideband is related to the HR factor since the mean and variance of the Poisson distribution in Eq. 3.30 is S. It is, however, still possible that an optical lineshape possesses a ZPL even in the strong coupling regime [88].
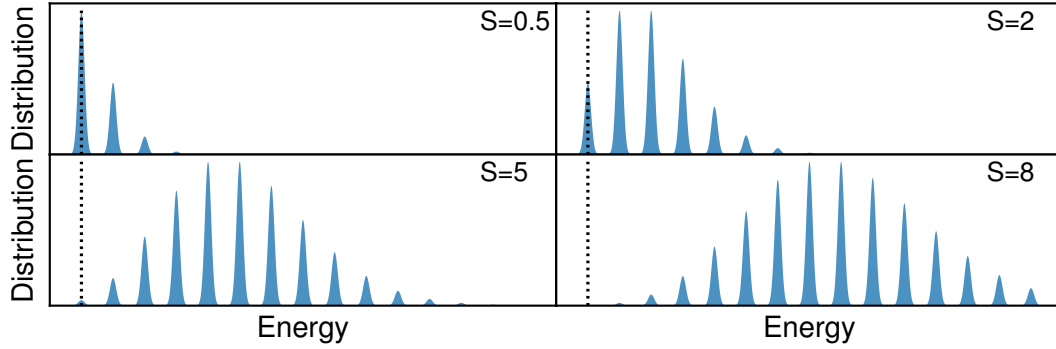

Figure 3.5: Poisson distribution for different values of the HR factor. The zero phonon line is indicated with a dotted black line.

3.3.2.3 Generating function method

The generating function method is a method to compute the intensity in Eq. 3.24 [8, 86, 88–90]. Here, the δ function is transformed to the time domain by the integral representation $\delta(\omega) = \frac{1}{2\pi} \int dt \, \exp(i\omega t)$. The lineshape function becomes

$$F(\omega) = (2\pi)^{-1} \int dt \, \sum_f \langle \chi_i | \chi_f \rangle \exp[i(E_f - E_i \pm \omega)t]. \tag{3.31}$$

It has been shown that under the approximations specified in Sect. 3.3.2.2 the *emission* lineshape function takes the following form [9, 88]

$$F(\omega_{\text{ZPL}} - \omega) = (2\pi)^{-1} \int dt \, \exp(i\omega t) \left[\exp\left(\int d\omega S(\omega) \exp(-i\omega t) - S \right) \right]. \tag{3.32}$$

3.3.2.4 Broadening

Broadening of the emission lineshape can be divided into two classes. Homogeneous broadening, which arises due to increased temperature, and inhomogeneous broadening. Inhomogeneous broadening is the broadening that results, e.g., from measuring

on an ensemble of defects with slightly different local environments such that the transition energy is slightly different [91]. These differences in local environments could caused by the presence of other types of defects or interfaces.

3.3.2.5   Inverse participation ratio

The inverse participation ratio is defined as [9]

$$\mathrm{IPR}_v = \left[\sum_a \langle \eta_{a,v} | \eta_{a,v} \rangle \right]^{-1}. \tag{3.33}$$

It measures the number of atoms that participate in the vibrational motion. Here, $\eta_{a,v}$ is the displacement of atom a in phonon mode v. The value of the inverse participation ratio may vary between 1 and the number of atoms in the computational supercell.

4

First-principles methodology

4.1 Background

The Hamiltonian for a system composed of electrons and nuclei is

$$H(\{\mathbf{r}\}, \{\mathbf{R}\}) = -\frac{1}{2} \sum_i \nabla_i^2 - \frac{1}{2} \sum_j M_j^{-1} \nabla_j^2 - \sum_i \sum_j \frac{Z_j}{|\mathbf{r}_i - \mathbf{R}_j|} + \sum_i \sum_{j>i} \frac{1}{|\mathbf{r}_i - \mathbf{r}_j|}, \qquad (4.1)$$

where i runs over electrons, j runs over ions and Z_j (M_j) is the nuclear charge (mass) of ion j. The solutions to Eq. 4.1 are many-body wave functions accounting for both electronic and ionic degrees of freedom. It is infeasible to compute the wave function for any realistic system, with the exception of the simplest molecular systems, due to the many degrees of freedom.

A standard approximation in order to simplify Eq. 4.1 is the Born-Oppenheimer approximation. In the Born-Oppenheimer approximation the nuclear and electronic degrees of freedom are separated. This separation is justified by the large mass difference between nuclei and electrons. The separation of variables yields the following two Hamiltonians for electronic and ionic degrees of freedom

$$H_{\text{electron}}(\{\mathbf{r}\}; \{\mathbf{R}\}) = -\frac{1}{2} \sum_i \nabla_i^2 - \sum_i \sum_j \frac{Z_j}{|\mathbf{r}_i - \mathbf{R}_j|} + \sum_i \sum_{j>i} \frac{1}{|\mathbf{r}_i - \mathbf{r}_j|}, \qquad (4.2)$$

$$H_{\text{ion}}(\{\mathbf{R}\}; n) = -\frac{1}{2} \sum_j M_j^{-1} \nabla_j^2 + \varepsilon_n(\{\mathbf{R}\}). \qquad (4.3)$$

Here, H_{electron} depends parametrically on the ion coordinates and H_{ion} depends parametrically on the electron state as indexed by n.

Methods to solve for the eigenvalues and eigenvectors of H_{electron} were developed already in the 1930ies in the form of the Hartree and Hartree-Fock methods. Hartree-Fock is a wave function based method in the sense that the nonlinear Hamiltonian is constructed via an approximate many-body wave function. The Hartree-Fock method attempts to solve the Schrödinger equation with the Hamiltonian H_{electron} by explicitly including the exchange energy but completely neglecting the electron correlation energy. In general, the Hartree-Fock method is both expensive and inaccurate due to the lack of correlation energy, but elements of the method are still present in modern state-of-the-art electronic structure methods. For larger systems density based methods are more feasible due to the very large computational cost of wave function based methods.

4.2   Density functional theory

DFT is an in principle rigorous theory concerning the relation between the electron density and the observables (predominantly the total energy) of an electronic system exposed to an external potential. It is an established method, conceived in the 1960ies [92]. DFT offers a very good accuracy–cost ratio and is very popular in the field of condensed matter physics where it is habitually applied in studies of phenomena pertaining to the electronic structure. In practice, the method suffers from several inherent limitations such as the band gap problem but due to the popularity of the method, many of these shortcomings have been explored and are relatively well understood [5, 93].

4.2.1   The Hohenberg-Kohn theorems

From the nuclear arrangement, the many-body wave function is determined, which in turn determines the electronic density of *all* electronic states and in particular the ground state. Hohenberg and Kohn showed in 1964 [92] that the ground state electron density uniquely determines the external potential, i.e., the total energy is a unique functional of the electron density.

This can easily be shown in the case of non-degenerate ground states by considering two different external potentials v_1 and v_2 (middle term in Eq. 4.2) that give rise to Hamiltonians H_1 and H_2, which otherwise would be the same. Let ϕ_1, and ϕ_2 be the ground state many-body wave functions. Now, assume that the electron density derived from both ϕ_1 and ϕ_2 gives the same external potential. The variational principle states that

$$\langle \phi_1 | H_1 | \phi_1 \rangle < \langle \phi_2 | H_1 | \phi_2 \rangle = \langle \phi_2 | H_2 + v_1 - v_2 | \phi_2 \rangle = E_2 + \int n_2(\mathbf{r})[v_1(\mathbf{r}) - v_2(\mathbf{r})]d\mathbf{r}. \quad (4.4)$$

Now we have the following two inequalities since there is nothing special about the in-

dices

$$E_1 < E_2 + \int n_2(\mathbf{r})[v_1(\mathbf{r}) - v_2(\mathbf{r})]d\mathbf{r} \qquad (4.5)$$

$$E_2 < E_1 - \int n_1(\mathbf{r})[v_1(\mathbf{r}) - v_2(\mathbf{r})]d\mathbf{r}. \qquad (4.6)$$

Summing them gives

$$0 < \int [n_2(\mathbf{r}) - n_1(\mathbf{r})][v_1(\mathbf{r}) - v_2(\mathbf{r})]d\mathbf{r}, \qquad (4.7)$$

and we have assumed that $v_1 = v_2$, which is a contradiction.

The energy is a functional of the electron density

$$E[n(\mathbf{r})] = F[n(\mathbf{r})] + \int v(\mathbf{r})n(\mathbf{r})d\mathbf{r}, \qquad (4.8)$$

where F is the universal functional (kinetic energy and electron electron interaction energy). There is a second Hohenberg-Kohn theorem that states that the ground state electron density minimizes the energy by virtue of the variational principle, i.e.,

$$E[n_{GS}(\mathbf{r})] \leq E[n(\mathbf{r})], \qquad (4.9)$$

if the electron density is consistent with an external potential (v-representable) [93].

4.2.2   Kohn-Sham method

In the Kohn-Sham approach [94], the interacting electron system in the true potential is reformulated as many non-interacting electrons (Kohn-Sham orbitals) in an effective potential. It is *assumed* that the electron density of the interacting electron system in the true potential can be represented as the electron density of the many non-interacting electrons in the effective potential [93]. The Kohn-Sham equations are

$$\langle \phi_i | -\frac{1}{2}\nabla^2 + v_{\text{eff}} | \phi_i \rangle = \varepsilon_i. \qquad (4.10)$$

The Kohn-Sham orbitals and the electron density are related as follows

$$n(\mathbf{r}) = \sum_i f_i \phi_i^\dagger(\mathbf{r}) \phi_i(\mathbf{r}), \qquad (4.11)$$

where f_i is the occupation number of ϕ_i . The effective potential in Eq. 4.10 can can be further decomposed in contributions from the external potential, the Hartree potential, and the exchange-correlation (XC) potential [93]

$$v_{\text{eff}}(\mathbf{r}) = v_{\text{ext}}(\mathbf{r}) + \int d\mathbf{r}' \frac{n(\mathbf{r}')}{|\mathbf{r} - \mathbf{r}'|} + \frac{\delta E_{\text{XC}}[n]}{\delta n(\mathbf{r})}. \qquad (4.12)$$

Due to the non-linearity of the effective potential, the Kohn-Sham equations have to be solved self consistently, usually with iterative methods. The two first terms in Eq. 4.12, the external potential and the Hartree potential, are easy to evaluate whereas the XC potential contains all complex many body interactions present in the system. This potential has been, and continues to be the subject of considerable research efforts in order to improve the predictions within the DFT framework [95].

4.2.3   Exchange-correlation potential

From the Kohn-Sham equations one can define the XC energy as the difference between the energy of the system and the known contributions from the external and Hartree potentials as well as the kinetic energy of the non-interacting states

$$E_{\text{XC}}[n] = E[n] - \int d\mathbf{r}\, v_{\text{ext}}(\mathbf{r})n(\mathbf{r}) - T[n] - v_{\text{H}}[n]. \tag{4.13}$$

The exact XC functional is not known and has to be approximated.

4.2.3.1   Local and semi-local functionals

The local density approximation (LDA) is one of the simpler XC approximations and represents the lowest step on the Perdew ladder of approximations to the XC energy [96]. Both the exchange energy and the correlation energy are obtained from the corresponding energy density of the homogeneous electron gas, i.e.,

$$E_{\text{XC}} = \int d\mathbf{r}\, n(\mathbf{r})[\epsilon_{\text{X}}^{\text{HEG}}(n(\mathbf{r})) + \epsilon_{\text{C}}^{\text{HEG}}(n(\mathbf{r}))]. \tag{4.14}$$

The exchange energy of the homogeneous electron gas has a closed form whereas the corresponding correlation energy has been be obtained from quantum Monte Carlo simulations [97] that was then used to fit a function for the correlation energy [98].

Semi-local functionals within the generalized gradient approximation (GGA) are more complex in comparison with the LDA. Besides the electron density, the XC functional depends on the magnitude of the generalized gradient of the electron density. And while the gradient is in principle a local quantity, the additional dependence of the infinitesimal surrounding region renders the gradient dependent functionals semi-local in nature. The dependence on the variation of the electron density provides a better description of systems that exhibit a rapidly varying electron density and GGAs generally offer an improvement compared to the LDA. There are many GGA functionals and some of the more popular are PBE [99] and PBEsol [83], which have been utilized in some studies in connection to this thesis.

4.2.3.2 Van der Waals and non-local functionals

Local and semi-local functionals have some serious drawbacks, one of which is their inability to correctly describe dispersion interactions. This renders especially semi-local DFT futile for systems for which at least some important degrees of freedoms are dominated by weak dispersion interactions, e.g., bi- and multi-layer systems as well as vdW solids in general. LDA has a tendency to overbind atoms and modeling bilayers with the LDA can lead to seemingly sound results for the wrong reasons. There are several ways to include dispersion interactions in DFT, but the one used throughout the papers this thesis is the non local vdW-df-cx functional [71, 100]. While it is coined as a vdW functional, the vdW-df-cx functional has also been shown to accurately describe quantities in bulk solids such as lattice parameter, cohesive energies, and vibrational properties [64, 101]. The vdW-df-cx functional has been used in **Paper I** to describe the atomic geometry, in **Paper V**-**Paper VII** to model the geometry of the bilayer systems, and in **Paper VIII** to construct phase diagrams of monolayer alloys.

4.2.4 Self-interaction error

While the Hohenberg Kohn theorem asserts the exactness of DFT, in the practical Kohn-Sham method, local and semi-local XC functionals suffer from self-interaction errors in which electrons interact with themselves through the mean field. This leads, among other things, to a propensity for orbital delocalization. It has also been observed that methods that reduce the self-interaction error tend to improve the description of band gaps [102]. There are remedies for the self-interaction error in the form of DFT+U and hybrid functionals [93]. DFT+U is a method in which a Coulomb repulsion energy U is added to a particular state in order to correct the Coulomb interaction of the overly delocalized states of local or semi-local DFT.

4.2.4.1 Hybrid functionals

Hybrid functionals is a class of XC functionals that accounts for the exact-exchange energy to some degree by inclusion of the following non-local Coulomb matrix elements

$$M_{nm} = \int \int \frac{1}{|\mathbf{r} - \mathbf{r'}|} n^\dagger_{nm}(\mathbf{r}) n_{nm}(\mathbf{r'}) \, d\mathbf{r} d\mathbf{r'}, \qquad (4.15)$$

where n_{nm} is the orbital density of Kohn-Sham states ϕ_n and ϕ_m. The exchange energy is then a sum over the occupied states

$$E_X^{exact} = -\frac{1}{2} \sum_{n,m} M_{nm} \qquad (4.16)$$

If one were to only include the exact-exchange energy in the XC energy one would obtain a Hartree-Fock calculation, in which there is no self-interaction by construction.

Hence, hybrid functionals provide a remedy for systems that critically suffer from the self-interaction error. By mixing in a quarter of the exact-exchange energy, the PBE0 functional is obtained [103]

$$E_{\text{XC}} = \frac{1}{4}E_{\text{X}}^{\text{exact}} + \frac{3}{4}E_{\text{X}}^{\text{PBE}} + E_{\text{C}}^{\text{PBE}}. \tag{4.17}$$

The range-separated HSE06 functional [104, 105] is obtained by decomposing the exchange energy in a short and long-ranged part and only apply the exact-exchange energy for the short range part, keeping the full long-range exchange energy of PBE.

$$E_{\text{XC}} = \frac{1}{4}E_{\text{X}}^{\text{SR, exact}} + \frac{3}{4}E_{\text{X}}^{\text{SR, PBE}} + E_{\text{X}}^{\text{LR, PBE}} + E_{\text{C}}^{\text{PBE}}. \tag{4.18}$$

For implementations in periodic DFT, the orbital densities n in Eq. 4.15 carries a nonzero phase and the exact-exchange energy in Eq. 4.16 becomes an integral over the first Brillouin zone. While hybrid functionals may offer an improved description of certain quantities over local, or semi-local DFT, for plane-wave basis sets, hybrid functionals are significantly more expensive than semi-local DFT due to the explicit evaluation of the non-local Coulomb matrix elements, which scales badly with both electron count and density of the Brillouin zone sampling from a computational perspective.

4.2.5 Charged systems

Models of crystalline systems require periodic boundary conditions. While a real crystal is charge neutral on average, theoretically one can consider charged systems by modifying the number of electrons. This will have the effect that the system consists of an infinite array of charged cells. The standard method to avoid a divergence in the electrostatic energy is to add a compensating background charge based on the Jellium model so that the computational cell is charge neutral on average. Localized charge will however still interact with its periodic image. This will have the effect that the formation energy of a localized charged defect is dependent on the size of the system beyond elastic interactions, which entails additional considerations when modeling the dilute limit formation energy of a charged defect.

There are two principal methods to handle the finite size corrections, *i*) a correction scheme based on material and supercell parameters, and *ii*) extrapolation by considering a set of supercells. Methods to account for image charge interactions has been developed [106, 107] based on the electrostatic interactions and Lany and Zunger suggested the following form of the correction scheme [107]

$$E_C = \frac{Mq^2}{3L\varepsilon}, \tag{4.19}$$

where M is the Madelung constant and L is the cell length. For periodic 2D systems, which exhibits a mix of different types of screening, extrapolation has been suggested

as a feasible route to handle the finite size effects [108, 109]. Since the out-of-plane direction is essentially unscreened, special supercells with a specific amount of vacuum was shown to facilitate the extrapolation.

The standard method to model isolated defects in semiconductors/insulators is by using super cells. The relation between the super cell cell metric and the unit cell cell metric is given by

$$\mathbf{A}_{sc} = \mathbf{T}\mathbf{A}_{uc}, \tag{4.20}$$

where $\mathbf{T}$ is a transformation matrix. A practical consideration for anisotropic unit cells is that a simple integer repetition (diagonal transformation matrix) is likely to result in a non-optimal supercell. In the worst case, a non-optimal supercell would lead to that the defect periodic image distance is much smaller in one direction compared with the other. This can be mediated by considering the full transformation matrix between the unit cell and the supercell and optimizing the transformation matrix such that the target supercell is as cubic as possible [110].

4.2.6 Excited states

Charge neutral excitations can be modelled by the ΔSCF method [93], in which the occupation numbers are constrained. This method explicitly accounts for the difference in character between the ground state and excited state in the construction of the electron density. The atomic geometry of the excited state can be obtained by relaxing the structure with the constrained occupations that corresponds to the excited state.

4.2.7 Projector augmented wave method

The othogonality requirement for the single particle states implies that the valence states must vary rapdily in the core region. From a computational perspective this entails that very high Fourier components must be used in a plane wave expansion of the single particle valence wave function. The idea with the projector augmented wave [111] method is that one can divide space into a core region and a valence region and obtain the ground state energy based on pseudo wave functions. These are related to the wave function by a linear transformation. In this case, the full structure of the wave function close to the atoms is, or can be retained, which is not the case for e.g. pseudopotentials. This makes the projector augmented wave method more accurate compared with pseudopotential methods that does not preserve information about the wave function in the core region.

The single particle pseudo wave function, which is smooth in the core regions is related to the single particle wave function as $\psi_{nk} = U\tilde{\psi}_{nk}$. The transformation U is of the following type

$$|\psi_{nk}\rangle = \left(1 + \sum_{a} s_a\right)|\tilde{\psi}_{nk}\rangle, \tag{4.21}$$

with $s_a = 0$ for $|r - r_a| > r_{\text{cutoff}}$. The rationale for a transformation of this type is that $\langle r|\psi_{nk}\rangle$ and $\langle r|\tilde{\psi}_{nk}\rangle$ coindices for $|r - r_a| > r_{\text{cutoff}}$ and that the augmentation spheres form a spatially disjoint set [111, 112]. Within the augmentations spheres the wave function can be expanded in a complete basis set $\{\phi_i^a\}$, which is related to the pseudo basis set $\{\tilde{\phi}_i^a\}$, via the transformation U. This gives

$$s_a|\tilde{\phi}_i^a\rangle = |\phi_i^a\rangle - |\tilde{\phi}_i^a\rangle. \qquad (4.22)$$

For augmentation sphere a [112]

$$\tilde{\psi}_{nk} = \sum_i \langle p_i^a|\tilde{\psi}_{nk}\rangle|\tilde{\phi}_i^a\rangle, \qquad (4.23)$$

where p_i^a are the projector functions, which satisfies $\langle p_i^a|\tilde{\phi}_j^a\rangle = \delta_{i,j}$. The transformation U has then the explicit form of [111]

$$U = 1 + \sum_a \sum_i (|\phi_i^a\rangle - |\tilde{\phi}_i^a\rangle)\langle p_i^a|. \qquad (4.24)$$

The energy of the system is then found from the stationary Schrödinger equation and a transformed hamiltonian. The projector augmented wave method as implemented in GPAW [113, 114] and VASP [115–117] has been used for DFT calculations in the studies this thesis is based on. For the studies in **Paper VI**-**Paper VII**, the explicit evaluation of matrix elements within the projector augmented wave formalism was implemented in the GPAW framework.

4.3 Beyond density functional theory

4.3.1 *GW* approximation

The *GW* approximation is a many-body method to compute the quasi-particle spectra of a set of interacting electrons [118] by expanding the self energy in the screened Coulomb interaction $W = \epsilon^{-1}v$.

The equation of motion for a quasi particle in an external potential is [119]

$$\left[-\frac{1}{2}\nabla^2 + v_H(\mathbf{r}) + v_{\text{ext}}(\mathbf{r})\right]\psi_i(\mathbf{r}, E) + \int d\mathbf{r}'\, \Sigma(\mathbf{r}, \mathbf{r}', E)\psi_i(\mathbf{r}') = \varepsilon_i(E)\psi_i(\mathbf{r}, E), \qquad (4.25)$$

where the one-electron self-energy Σ is a *i)* non local *ii)* energy dependent *iii)* complex valued potential that accounts for the XC interactions. The self-energy expressed in the many-body Green's function is [120]

$$\Sigma(\mathbf{r}, \mathbf{r}', E) = G_0^{-1}(\mathbf{r}, \mathbf{r}', E) - G^{-1}(\mathbf{r}, \mathbf{r}', E), \qquad (4.26)$$

where G is the Greens function

$$G(\mathbf{r}, \mathbf{r}', E) = \sum_i \frac{\psi_i(\mathbf{r}, E)\psi_i^\dagger(\mathbf{r}', E)}{E - \varepsilon_i(E)}. \tag{4.27}$$

G_0 is the corresponding Green's function for the case of $\Sigma = 0$. It was shown by Hedin [118] that the lowest order expansion of the self energy in the screened Coulomb interaction W is the GW term i.e. [119]

$$\Sigma(\mathbf{r}, \mathbf{r}', E) = (-2\pi i)^{-1} \int dE' G(\mathbf{r}, \mathbf{r}', E + E')W(\mathbf{r}, \mathbf{r}', E'). \tag{4.28}$$

The GW approximation is in principle not connected to the theoretical framework of DFT. However, quasi-particles from DFT can be used to construct the initial states in the GW approximation. Due to intricate dependencies between the screened Coulomb interaction and the Green's function, the self energy must be computed iteratively. However, GW calculations are computationally demanding and one common shortcut is the G_0W_0 approximation, where the Green's function in Eq. 4.28 is replaced by G_0 and the screened interaction by W_0 (evaluated based on G_0) [121]. The G_0W_0 method provides a correction to the quasi-particle levels of conventional DFT, but as any perturbative method, the quasi-particle levels depend on the underlying DFT computations [122]. Note that the sum over states in Eq. 4.27 is not restricted to occupied states, and hence describes the full quasi-particle spectrum.

The dielectric function exhibits a very different behavior in the long-wavelength limit of 2D compounds compared with a 3D compound, e.g., the dielectric constant tends to 1 in the long-wavelength limit for 2D materials [123, 124]. It is difficult to converge (with respect to vacuum) the quasi-particle levels in a G_0W_0 calculation of a monolayer using periodic boundary conditions in the out-of-plane direction. Hence, some truncation of the Coulomb interaction should be necessary in order to accurately determine the band gap of 2D materials with G_0W_0 [124]. However, in **Paper V**, we were interested in the relative band gap difference when displacing monolayers relative to each other, a quantity that converges much faster with added vacuum than the absolute band gap.

4.4 Phonons

4.4.1 Theory of small oscillations

The atoms move much slower than the electrons so the Hamiltonian for the atoms is

$$H(\{\mathbf{R}; n\}) = -\frac{1}{2}\sum_j M_j^{-1}\nabla_j^2 + E_n(\{\mathbf{R}\}). \tag{4.29}$$

n is here a quantum number indicating the electronic state of the system. Here we are concerned with the electronic ground state. The harmonic vibrations of the atoms in a general crystal can be described with a semi-classical model comparable to the equations of motion of a set of beads connected with springs. To find the proportionality constants between the force and the displacement the total energy relative to the equilibrium energy is expanded in a basis of small atomic displacements.

The equilibrium position of atom i is

$$\mathbf{r}_{il} = \mathbf{p}_l + \mathbf{q}_i, \tag{4.30}$$

where $\mathbf{p}_l$ is the translation vector to unit cell l and $\mathbf{q}_i$ is the relative position of atom i in unit cell l. A small displacement of atom i in unit cell $\mathbf{p}$ relative to its equilibrium position is

$$\mathbf{u}_{il} = \mathbf{p}_l + \delta\mathbf{q}_i - \mathbf{p}_l + \mathbf{q}_i. \tag{4.31}$$

The Taylor expansion can be written as

$$E(\{\mathbf{u}\}) \approx \frac{1}{2} \sum_{i'l'} \sum_{il} \sum_{\alpha,\beta} \frac{\partial^2 E}{\partial u_{il}^\alpha \partial u_{i'l'}^\beta}\bigg|_0 \cdot u_{il}^\alpha u_{i'l'}^\beta, \tag{4.32}$$

where α and β index the Cartesian components of the displacement vector. The zeroth order term is the reference energy, and the first order term vanishes via the definition of the equilibrium positions. The quantity

$$\Phi_{il,i'l'}^{\alpha\beta} = \frac{\partial^2 E}{\partial u_{il}^\alpha \partial u_{i'l'}^\beta}\bigg|_0 \tag{4.33}$$

is called a *second-order* force constant, and measures the force extereted on atom il when atom $i'l'$ is displaced. Now, i is bound in crystalline systems, whereas l is unbounded due to an infinite repetition of unit cells. In practice, the second-order force constants decay relatively fast with the distance ($|\mathbf{r}_{il} - \mathbf{r}_{i'l'}|$) due to screening of the induced fields. Therefore, the number of unit cells that has to be included in the energy expansion is system dependent. The analytic property of the energy as a function of displacement is an assumption, which may be violated in some cases. There may be long range interactions that are not captured in the energy expansion, which however can be handled using non analytical corrections. These are dipole dipole interactions in polar materials that gives rise to the well known energy splitting between longitudinal and transverse optical phonon modes.

The harmonic Hamiltonian is [90]

$$H = -\frac{1}{2} \sum_j M_j^{-1} \nabla_j^2 + \frac{1}{2} \sum_{i'l'} \sum_{il} \sum_{\alpha,\beta} \Phi_{il,i'l'}^{\alpha\beta} \cdot u_{il}^\alpha u_{i'l'}^\beta. \tag{4.34}$$

The *second order* force constants are used to construct the dynamical matrix [10]

$$D_{ii'}^{\alpha\beta}(\mathbf{q}) = \frac{1}{\sqrt{m_i m_{i'}}} \sum_{l'} \Phi_{i0,i'l'}^{\alpha\beta} \exp(i\mathbf{q} \cdot [\mathbf{r}_{i0} - \mathbf{r}_{i'l'}]). \qquad (4.35)$$

The eigenvalues of the dynamical matrix are the squared frequencies.

4.4.2   Computational method

To compute the phonon frequencies and eigenvectors, the most straightforward approach is the so-called frozen phonon approach, where the atoms of system are displaced and the energy is computed and subsequently the second-order force constants, see Eq. 4.33. The only requirement of the underlying electronic structure code is to be able to evaluate the total energy of a system. In practice, numerous software packages, e.g., phonopy [10] are interfaced with modern electronic structure codes that facilitate the computations by providing the relevant input, i.e., the symmetry reduced displacements, and parsing the relevant output.

The drawback of the frozen phonon approach is that the number of displacements can be an unfeasible large number, specially for low-symmetry systems such as defects. In principle, a full DFT calculation is required for each symmetry inequivalent degree of freedom. Another approach, which is based on regression is to make simultaneous displacements and fit the set of force constants to the forces from the DFT calculations [11].

5

Oxygen vacancies in wide band gap oxides

In this chapter, the findings pertaining to oxygen vacancies are presented. This chapter also serves as a summary of **Paper I** and **Paper II**.

5.1   Alignment of defect levels

In **Paper I** we address **Q1** of the introduction, which is here repeated for convenience.

> **Q1.** Is it possible to understand the properties of oxygen vacancies in wide band gap oxides without having to explicitly study the oxygen vacancy in each new oxide?

One of the most important features of a defect is the CTL and for oxygen vacancies the most relevant CTL is the $(0/+2)$ CTL. Therefore, when addressing **Q1** we considered the $(0/+2)$ CTL of 26 different wide band gap oxides, of which there were 6 ternary oxides (perovskite oxides) and 20 binary oxides. The oxides considered were

- AO, A = Be,Mg,Ca,Sr,Ba,Zn,

- ABO_3, A = Ba,Pb and B = Ti,Zr,Hf,

- AO_2, A = Ti, Si, Sn, Hf,Zr, Ge,

- A_2O_3, A = Al,Ga,In,Sc,Y,Lu.

These oxides are of closed shell type (Sect. 2.1.1.1) and exhibits a plethora of different crystal structures (e.g., perovskite, rock salt, and bixbyite) and a large variation in band

gaps. Furthermore, there is a large variation in the coordination of the oxygen atoms over the considered oxides as is indicated by the different stoichiometries. The defect calculations were performed with conventional DFT using the vdW-df-cx functional [71] in order to obtain the atomic geometry. Subsequently, the HSE06 hybrid functional [104, 105] was used to compute the energetics without allowing for atomic relaxation.

In order to assess general features of the oxygen vacancies using the CTLs, these have to be compared on an absolute scale. To this end, the band edges were aligned to the oxygen $1s$ level. This level presumably does not participate in the formation of metal-oxygen bonds and therefore probes mainly the local electrostatic environment. The band alignment of the considered oxides closely resembles the common anion rule with a few exceptions.

The main finding of **Paper I** is that when the band edges are aligned to a common reference level, the $(0/+2)$ CTL exhibits a common value of -5.2 eV with a standard deviation of 0.7 eV. This is a indication of a commonality of the oxygen vacancies due to the large span of band gaps in the considered oxides. The main feature that determines the character of the oxygen vacancy i.e. if the oxygen vacancy is shallow or deep (Sect. 3.2) is the position of the conduction band with respect to the vacuum level. If the conduction band edge falls below around -5 eV, the oxygen vacancy could be shallow and otherwise it is likely deep.

In order to expand on the underlying physical origin we considered the potential of the oxygen vacancy and found that the "size" of the oxygen vacancy is similar in all these materials. The energy levels of a particle-in-box model is completely determined by the size of the box and we propose that this is the explanation for the almost constant CTL of oxygen vacancies in wide band gap oxides as well.

5.2 The three hallmarks of deep oxygen vacancy levels

In **Paper I**, the properties of oxygen vacancies in charge transfer oxides are examined and it is revealed that there are three common features for deep oxygen vacancy states. Deep oxygen vacancies exhibit the following features

  i) quasi-particle (Kohn-Sham) level in the band gap,

  ii) The $(0/+2)$ CTL resides in the band gap,

  iii) Large structural distortion between different charge states.

The presence of a Kohn-Sham level in the band gap is a clear indication that a mid gap state is formed while feature *ii*) is in principle the definition of a deep defect level. Features *i*) and *ii*) are, however, subject to systematic errors within DFT, and may not al-

ways be observable. For example, due to the underestimation of the band gap, both the $(0/+2)$ CTL and the Kohn-Sham level may be erroneously positioned above the conduction band edge.

In the case of vacancies in ionic materials, as is the case here, the structural distortion may be a good descriptor of the character of the defect state (Fig. 5.1).
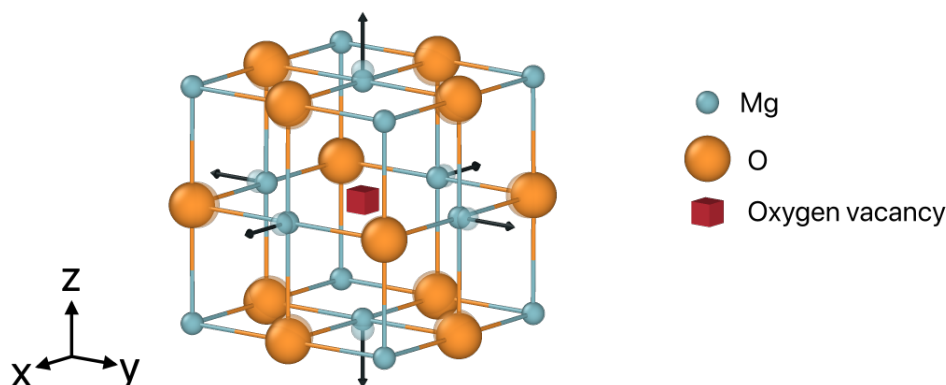

Figure 5.1: Structural distortion upon a change in charge state on the oxygen vacancy in MgO. The arrows depict the relaxation of the nearest Mg atoms between the neutral and doubly charged states. The solid color indicates atoms in the neutral charge state and the transparent atoms are those in the doubly charged state.

Many of these materials exhibit a strong ionic bonding character, which, in the ionic limit makes the oxygen atom doubly negatively charged. For the deep neutral oxygen vacancy there is a surplus of two spin-paired electrons that are predominantly localized in the vacancy. The geometry of the local environment of a neutral oxygen vacancy is relatively similar to the one of the vacancy-free structure due to the electronic screening provided by the electrons. For the $+2$ charged oxygen vacancy, these electrons are absent from the vacancy and the metal ions are now subject to a mutual unshielded Coulomb interaction that results in atomistic relaxation. This is shown in Fig. 5.1 for the case of an oxygen vacancy in MgO. This indicates that the structural distortion is a very good probe for the character of the oxygen vacancy state.
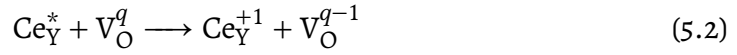
We are now in a position to give an answer to **Q1**. There are common features of the oxygen vacancy that extend over a variety of wide band gap oxides. The common features include a $(0/+2)$ CTL centered at -5.2 eV and the three hallmarks of deep oxygen vacancy levels discussed in this section.

5.3 Luminescence quenching

As discussed in the previous section, the structural distortion upon a charge state change on deep oxygen vacancies is associated with a lowering of the lattice energy, which is rel-

atively large. This fact underpins the exploration of possible recombination pathways in Ce:YAG that involves oxygen vacancies at some point. In order to address **Q2** of the introduction, in **Paper II** the CTLs of the oxygen vacancy were first evaluated and the CTLs indicate that the oxygen vacancy in YAG is deep. In order for the oxygen vacancy to be able to dissipate the excitation energy, the crucial step is electron transfer to the oxygen vacancy. Already at this step, luminescence is effectively quenched due to the depletion of the Ce:5d state.

Therefore, we considered the following three-step mechanism for non radiative recombination, starting from the charge states +1 or +2 of the oxygen vacancy.

$$\text{Ce}_\text{Y}^\times + \text{V}_\text{O}^q \xrightarrow{\hbar\omega} \text{Ce}_\text{Y}^* + \text{V}_\text{O}^q \tag{5.1}$$

$$\text{Ce}_\text{Y}^* + \text{V}_\text{O}^q \longrightarrow \text{Ce}_\text{Y}^{+1} + \text{V}_\text{O}^{q-1} \tag{5.2}$$

$$\text{Ce}_\text{Y}^{+1} + \text{V}_\text{O}^{q-1} \longrightarrow \text{Ce}_\text{Y}^\times + \text{V}_\text{O}^q \tag{5.3}$$

We assessed the energy barriers associated with each step in this mechanism and in order to validate our computations we modeled the optical lineshape of the Ce luminescence. Before continuing in describing the details of the reaction mechanism, the optical lineshape results are briefly presented. The generating function method was used to model the optical lineshapes and generally, a good agreement with experimental lineshapes is found. The fine structure observed in experiments [7] is shown to *not* be a result of local vibrational modes involving the nearest neighbor oxygen atoms. This is argued to be the case since there is no dominant mode in the electron phonon spectral function and the fine structure peaks are associated with low frequency phonon modes that likely originate from heavier atoms such as yttrium and not oxygen.

Having assessed the optical lineshape, which is related to the changes on the Ce$_\text{Y}$ atom in Eq. 5.1 we find that the charge transfer to the oxygen vacancy (Eq. 5.2) is associated with a minuscule energy barrier in the case of $q = +2$ and a negative barrier in the case of $q = +1$. The limiting step for the recycling of the oxygen vacancy as a quenching center is the transfer of the electron from the oxygen vacancy back to the Ce:4f state. This barrier is 0.8 eV in the case of $q = +1$. We estimated the energy barriers for thermal ionization and landscape crossover to 1.1 eV and 3.8 eV, respectively. The relatively low energy barrier suggests that out of these considered mechanisms, the proposed charge transfer mechanism is likely to be contributing to the thermal luminescence quenching.

The mechanism described in Eq. 5.1-5.3 depends mainly on the energetics of the oxygen vacancy, and is as such perhaps applicable to other oxide based phosphors as well. Based on the findings in **Paper II**, the answer to **Q2** is a short and simple yes.

<div align="right">

6

</div>

Color centers in h-BN and 4H-SiC

A defect exhibits multiple characteristic features including CTLs and formation energies. Optically active defects exhibit in addition vibrationally induced characteristics such as HR-factor, Stokes shift, and optical lineshape. In **Paper III** and **Paper IV**, we used the generation function approach to compute the emission lineshapes of defects in 4H-SiC and monolayer h-BN in order to compare and identify defects reported in literature based on the vibrationally induced properties.

6.1 Color centers in 4H-SiC

Paper III is concerned with defects in 4H-SiC. The following defects, heavily focused around the silicon vacancy (V_{Si}), were considered V_{Si}, $V_{Si}N_C$, $V_{Si}V_C$, V_CC_{Si}, and $V_{Si}N_C$, and in all 9 different transitions. The geometries of the defects and the vibrational spectra were obtained using the PBEsol functional. The ZPLs were computed using the hybrid functional HSE06 without allowing for further relaxation and the ZPLs fall between 0.72 eV and 1.69 eV, i.e. the infrared part of the spectrum and even the telecom region ($\approx$1 eV). We show that the emission lineshape of all these defects exhibit structure and a well defined phonon sideband with HR factors between 1.5 and 3.8. All considered emission lineshapes exhibit essentially zero intensity at energies of 400 meV above the ZPL relative to the phonon sideband peak with the exception of the carbon vacancy based V_CC_{Si} defect. This defect has a much longer tail than the defects based on V_{Si} and the largest HR factor of the considered defects at 3.8. It is found that there is a phonon band gap in defect free 4H-SiC between 75 meV to 90 meV that is to some extent preserved in the defective structures. In the region around 75 meV and above the electron phonon coupling for all considered defects attains a more local character and fewer atoms are

involved in the coupling to the electronic transition, revealing a commonality in the electron phonon coupling.

6.2 Color centers in h-BN

In **Paper IV**, conventional DFT was used to compute the geometry of the defect in the ground and excited states as well as the vibrational spectrum for the defective supercell. In addition, the hybrid functional HSE06 was used to estimate the transition energies for *charge* transitions, which inevitably suffers from the band gap problem present in conventional DFT.

A set of defects including both intrinsic defects and carbon based defects were considered. One common feature of many experimentally observed emission centers in h-BN is that the emission lineshape is structured with well defined phonon sidebands and thus exhibit a moderate HR factor. We find that, among the defects that can host transitions with moderate HR factors, carbon based defects and the negatively charged boron vacancy (V_B^{-1}) are the most likely candidates based on the HR factor. The electronic structure of V_B^{-1} is complex with several in-gap states including both occupied and unoccupied states. Two geometries of the excitation of the lowest unoccupied state on V_B^{-1} were investigated, D_{3h}, and C_{2v}. The D_{3h} state exhibit a threefold rotational symmetry and exhibit a weak electron phonon coupling with a HR factor of 0.9. The phonon sideband has a peak at 162 meV. The C_{2v} is distorted along one direction and exhibits a larger HR factor of 2.5 and consequently a wider phonon sideband.

Charge transitions on the carbon substitional defects C_N and C_B exhibit HR factors of 1.8-1.9 and consequently structured emission lineshapes with well defined phonon sidebands and associated phonon replicas. The analysis of the electron phonon coupling shows that it is predominantly modes at around 185 meV that contribute to the phonon sidebands for these transitions. The optical transition on $C_B C_N$ (i.e. neigbouring C_N and C_B) exhibit a similar lineshape as C_N and C_B, with the first phonon sideband located at 195 meV. The origin of the phonon sideband in $C_N C_B$ is a localized phonon mode that involves the breathing motion of the carbon atoms. In addition, we predicted a difference of 4 meV in the phonon sidebands for the $C_B C_N$ defect consisting of ^{13}C instead of the naturally occurring ^{12}C, which could help identifying this defect center experimentally.

To answer **Q3** of the introduction, we have predicted the phonon sidebands of several transitions/defects in h-BN and SiC and found that there are multiple defects that can host transitions with similar emission lineshapes. This makes an unambiguous identification based *only* on the computed shape of the emission spectrum not viable in general. It is however another accessible (from first-principles calculations) characteristic, together with e.g., ZPL, formation energy, spin state, electronic structure, Stokes shift, and HR factor that can be used to elucidate the chemical nature of emission centers.

7

Optical properties of TMDs

In this chapter, the results from the studies on untwisted and twisted TMD bilayers are addressed as well as the properties of TMD alloys. This section serves as a summary of **Paper V-VIII**.

7.1   Excitons in twisted bilayers

Twisting one monolayer in a bilayer structure induces certain structural distortions in comparison with the untwisted bilayer. In **Paper VII**, these structural distortions are investigated in detail for twisted MoS_2/MoS_2 down to a twist angle of 4.4°. The main structural distortions occurs in the binding distance due to the formation of regions of different stacking orders (Fig. 2.8) and the interlayer distance becomes ambiguous due to the spatial variation and attains the form of a distribution. We show that the distribution becomes very narrow at large twist angles (13.2°) centered at the mean value of the interlayer distance found in R_h^h and R_h^M. For smaller twist angles, the distribution becomes wider and the boundary points tends towards the interlayer distance in the limiting structures. In-plane structural distortion is observed as well with magnitudes around 0.2 Å for larger twist angles (7.3°) and around 0.6 Å for smaller twist angles (4.4°).

In **Paper V**, the influence of the twist induced potential on the inter- and intralayer excitons at the K-point is investigated for the $MoSe_2/WSe_2$ heterostructure in the low angle limit. Here, the intra and interlayer band gap variation of the limiting structures are computed using the G_0W_0 method. The G_0W_0 band gap variations were used in constructing a model based on the exciton density matrix formalism. The band gap variation is approximately equal to the electrostatic moiré potential at the K-point. In **Paper VI**, it is shown that the degree of hybridization or tunneling for both the conduction band and valence band is small at the K point. For small tunneling rates the interlayer

band gap variation from the G_0W_0 probes mainly the variation of the electrostatic potential. Furthermore, the small tunneling rates implies that hybrid intra/interlayer excitons is unlikely to be formed. In **Paper V**, it is shown that the twist induced potential has a profound effect on the exciton landscape. For very low twist angles, below 2° both the intra- and interlayer excitons becomes localized in space and at 3° the excitons obtain a delocalized form. For 1°, the interlayer exciton absorption spectra exhibit much more structure with at least four distinct peaks with alternating polarization. This is in contrast with the case of 3° where there are only two peaks in the absorption spectrum. In addition, for the case of 3° twist angle the intralayer absorption spectrum exhibit a single peak for each layer whereas for 1° twist angle this single peak is splitted into four peaks. In the introduction the following question was posed

Q4. How are the optical properties of a TMD bilayer affected by twisting one of the constituent monolayers?

This is a very complex question and a partial answer is that the ground state $K - K$ intra- and interlayer exciton becomes localized at twist angles below 2° and fine structure in the absorption spectrum appears due to the presence of the moiré potential.

The twist induced electrostatic potential in bilayer TMDs can be investigated by DFT calculations, and was done so in **Paper VII** to address question **Q6**. First, the limiting structures were considered and it was found that the induced electrostatic potential is an alternating dipolar potential, which originates from a charge displacement in asymmetric stacking orders. The magnitude of this dipolar potential is relatively similar across the TMDs H-MX_2 with M=Mo,W and X=S,Se,Te with a value of 131 meV and a standard deviation of 8 meV. Furthermore, in order to access the twist induced electrostatic potential in moiré superlattices with a finite twist angle, the electrostatic potential at the ion cores were considered. It was found that the amplitude of this electrostatic potential decays rapidly with increasing twist angle. For the 4.4° twisted MoS_2/MoS_2 bilayer, the amplitude at ~ 5° is about half of the 0° value. The twist angle dependence of the potential is attributed to twist angle dependence of both the interlayer spacing and the interlayer horizontal alignment that determines the induced dipole moment. The results in **Paper VII** on the twist induced potential suggests that charge carrier transport is subject to a twist angle dependent energy barrier that might impede charge carrier transport and the associated exciton transport.

7.2   Untwisted bilayers

The intra- and interlayer excitons at the $K - K$ point in $MoSe_2$/WSe_2 could be modeled using band gap variations due to negligable tunneling rates at that particular point in the Brillouin zone. Other excitons, including hybrid excitons require additional efforts.

In **Paper VI** and **Paper VII** the disentanglement of the electrostatic potential and hybridization energy is undertaken in order to answer **Q5** posed in the introduction. The magnitude of the hybridization and dipole potential in both TMD homobilayers and TMD heterobilayers are determined for the limiting structures. The disentaglement between hybridization and electronic state realignment is achieved by solving the Poisson equation for the electron density difference and then subtract the electronic state realignment from the energy of the electronic states of the bilayer. The electronic state realignment is found by computing the following matrix element, with the potential coming from the electron density difference

$$M = \langle \psi_{n\mathbf{k}} | \delta V | \psi_{n\mathbf{k}} \rangle. \tag{7.1}$$

The electronic states of the bilayer contains both hybridization and electronic state realignment. The valence band, which presumably is involved in the electronic density displacement is strongly hybridized in a small region around the zone center for all considered materials, whereas hybridization in the conduction band is strongest at the Λ point.

The electronic state realignment and momentum resolved hybridization energies were used in **Paper VI** to assess the lowest energy exciton in untwisted TMD homostructures and heterostructures by means of density matrix theory. The numerous systems that were considered, exhibited to a large extent different excitonic landscapes. For example, in all stacking orders, we found that the lowest energy exciton in MoS_2/MoS_2 homobilayer and MoS_2/WS_2 heterobilayer is an indirect exciton where the hole originates at the zone center and the electron at the K'-point. Whereas for WS_2/WS_2, the $K - \Lambda$ exciton is the lowest energy exciton in R_h^h and $\Gamma - \Lambda$ for the other stacking orders. For the selenides, the lowest exciton in the R stacked $MoSe_2/WSe_2$ heterobilayer is the $K - K$ exciton whereas the H stacked systems where indirect with the hole at K and the electron at either Λ or K'. In WSe_2/WSe_2 the lowest exciton were indirect ($K - \Lambda$) while in $MoSe_2/MoSe_2$ both indirect ($K - \Lambda$) and direct ($K - K$) excitons exhibited the lowest energy, depending on stacking order.

7.3 Monolayer TMD alloys

The main objective of **Paper VIII** was to determine the mixing properties and band edge alignment of TMD alloys. Here, DFT calculations in conjunction with cluster expansions and Monte Carlo simulations were used. To this end, the systems tabulated in Table 7.1 were considered. It was found that many TMDs exhibit an in-plane ordered ground state e.g., $Mo_xW_{1-x}S_2$, which is slightly lower in energy in comparison with the randomly mixed state. The critical temperatures for the ordered to disordered transitions were found to be very small (on the order of a few tens of K) in almost all

Table 7.1: Alloy systems considered in **Paper VIII**. Tuples indicate the mixing species.

Symmetry	Mixing site	Transition metals	Chalcogen species
H	X	Ti, Zr, Hf, Mo, W	(S,Se), (S,Te), (Se,Te)
T	X	Ti, Zr, Hf, Pd, Pt	(S,Se), (S,Te), (Se,Te)
H	M	(Ti, Zr), (Ti, Hf), (Ti, W), (Hf, Zr), (Hf, W), (Mo, Ti), (Mo, Zr), (Mo, W) (W, Zr), (Hf, Mo)	S, Se, Te
T	M	(Ti, Zr), (Hf, Ti), (Hf, Zr), (Pd, Pt)	S, Se, Te

systems with an ordered ground state with the exception of T-$HfS_{2x}Te_{2(1-x)}$ and H-$HfS_{2x}Se_{2(1-x)}$. These system exhibit ordered states stable up to around 100 K. This result indicate that in-plane ordered phases in TMD alloys are not present at ambient conditions. Furthermore, there were numerous systems that do not easily mix. These are found to predominantly consists of either chalcogen mixed alloys where S and Te are mixing as well as mixing of cations from different groups of the periodic table. In addition, cation mixed systems with Ti also exhibit large critical temperatures even if mixed with Zr and Hf, which are in the same group in the periodic table. The systems with mixing of cations from different groups exhibit the largest critical temperatures with values up to several thousands of K. Finally, the alloys $TiX_{2x}Te_{2(1-x)}$ with X=S, Se exhibit critical temperatures above room temperature. In **Paper VIII**, the software SISSO [125] was used to construct simple models of the critical temperature based on features from the boundary phases. For transition mixed alloys, a functional form that includes the difference in ionization potential and elastic energy predicts the critical temperature reasonable well. Furthermore, SISSO was used to classify the ground state of chalcogen mixed alloys as ordered, non-mixing, or Janus. It is found that two descriptors, one with units of pressure and one adimensional that is related to the bonding in the material can predict the category of the chalcogen mixed alloy with 93% success rate.

Many of the considered alloys exhibit extremely large critical temperatures and are excluded from further investigations into the electronic structure. The electronic band edges for a subset of the considered alloys were evaluated and aligned to the vacuum level. The bowing parameters were estimated using on conventional DFT calculations. The valence band edge bowing parameter was found to be negative for all chalcogen mixed alloys with an increasing magnitude in the series $S_{2x}Se_{2(1-x)}$, $Se_{2x}Te_{2(1-x)}$, $S_{2x}Te_{2(1-x)}$. In **Paper VIII**, we answer **Q7** by showing what TMDs alloys that are likely to mix and the possible variation in band edge energies due to different compositions.

8

Outlook

The studies this thesis is based on does not follow a straight red line with regards to the topic. Different materials have been studied, different physical processes have been modeled, and different issues have been addressed. What unites them however, is the topic of atomistic handicraft and the pursuit of understanding how materials act on the microscopic scale when the composition or orientation is manipulated. We are in the middle of an age where materials can be manipulated and controlled on the atomic scale to yield fantastically different behavior. Here, in this thesis, the chemical nature of defects that are presumed to be responsible for certain observed behavior such as emission lines or luminescence quenching in specific materials, are elucidated.

Some of these studies have been of high-throughput character where many materials or many defects have been addressed and hopefully these studies could serve as roadmaps for further experimental and theoretical investigations. On the theoretical side, there might be a paradigm shift coming with the advent of machine learning algorithms adjusted for problems in materials science, both for computing and for analysis [11, 125, 126]. This may have huge impact for establishing, and understanding trends and similarities across materials. Machine learning algorithms can help in establishing phenomenological models based on material specific features, which could elucidate what features that leads a specific property e.g., deep defect states in different related materials. There is a simple satisfactory explanation for the commonality of oxygen vacancies in **Paper I** in terms of band edge positions and size of the vacancy, however, in other situations it might become too difficult to find simple predictors by manual inspection.

There are numerous interesting directions for further studies on the topics covered in this thesis. It should be of interest to further investigate the ability of oxygen vacancies to act as non-radiative electron capture centers in order to understand the limitations of wide band gap oxide semiconductors in micro- and optoelectronical applications. Here the results from **Paper I** is a start, but modeling the electron dynamics require much

more effort. First-principles investigations of non-radiative carrier capture rates of important defects in e.g., GaP has been performed based on the generating function method so the method is already established [127]. The bottleneck is the computation of electron-phonon matrix elements, which may be difficult in oxides due to the strong ionic character that many oxides exhibit. Furthermore, the large structural distortion of charge transitions on oxygen vacancies in some materials may require treatment of anharmonicity.

The moiré potential was the subject of study for the exciton TMD papers and in all bits and pieces on how twisting influences the electronic properties has been revealed. Understanding that the underlying electrostatic moiré potential is of dipolar origin and originates from an asymmetric charge displacement opens up for interesting possibilities in tailoring this potential e.g., by applying pressure to decrease the interlayer distance or make moiré superlattices of Janus monolayers that already have an intrinsic dipole moment. This would perhaps make the moiré potential deeper and localize excitons at larger twist angles. Furthermore, in multilayer materials, there are additional twisting degrees of freedom and the electronic properties of twisted multilayer heterostructures is almost completely unexplored.

Acknowledgments

Bibliography

[1] P. Neumann, N. Mizuochi, F. Rempp, P. Hemmer, H. Watanabe, S. Yamasaki, V. Jacques, T. Gaebel, F. Jelezko, and J. Wrachtrup, *Multipartite Entanglement Among Single Spins in Diamond*, Science **320**, 1326 (2008). doi:10.1126/science.1157233.

[2] I. Aharonovich, D. Englund, and M. Toth, *Solid-state single-photon emitters*, Nature Photonics **10**, 631 (2016). doi:10.1038/nphoton.2016.186.

[3] Z. Xia, Z. Xu, M. Chen, and Q. Liu, *Recent developments in the new inorganic solid-state LED phosphors*, Dalton Transactions **45**, 11214 (2016). doi:10.1039/C6DT01230B.

[4] T. T. Tran, K. Bray, M. J. Ford, M. Toth, and I. Aharonovich, *Quantum emission from hexagonal boron nitride monolayers*, Nature Nanotechnology **11**, 37 (2016). doi:10.1038/nnano.2015.242.

[5] J. P. Perdew, *Density functional theory and the band gap problem*, International Journal of Quantum Chemistry **28**, 497 (1985). doi:10.1002/qua.560280846.

[6] J. Ueda, P. Dorenbos, A. J. J. Bos, A. Meijerink, and S. Tanabe, *Insight into the Thermal Quenching Mechanism for $Y_3Al_5O_{12}$:Ce^{3+} through Thermoluminescence Excitation Spectroscopy*, The Journal of Physical Chemistry C **119**, 25003 (2015). doi:10.1021/acs.jpcc.5b08828.

[7] V. Bachmann, C. Ronda, and A. Meijerink, *Temperature Quenching of Yellow Ce^{3+} Luminescence in YAG:Ce*, Chemistry of Materials **21**, 2077 (2009). doi:10.1021/cm8030768.

[8] M. Lax, *The Franck-Condon Principle and Its Application to Crystals*, The Journal of Chemical Physics **20**, 1752 (1952). doi:10.1063/1.1700283.

[9] A. Alkauskas, B. B. Buckley, D. D. Awschalom, and C. G. V. de Walle, *First-principles theory of the luminescence lineshape for the triplet transition in diamond NV centres*, New Journal of Physics **16**, 073026 (2014). doi:10.1088/1367-2630/16/7/073026.

[10] A. Togo and I. Tanaka, *First principles phonon calculations in materials science*, Scripta Materialia **108**, 1 (2015).

[11] F. Eriksson, E. Fransson, and P. Erhart, *The Hiphive Package for the Extraction of High-Order Force Constants by Machine Learning*, Advanced Theory and Simulations **2**, 1800184 (2019). doi:10.1002/adts.201800184.

[12] K. F. Mak, C. Lee, J. Hone, J. Shan, and T. F. Heinz, *Atomically Thin MoS_2: A New Direct-Gap Semiconductor*, Physical Review Letters **105**, 136805 (2010). doi:10.1103/PhysRevLett.105.136805.

[13] A. K. Geim and K. S. Novoselov, *The rise of graphene*, Nature Materials **6**, 183 (2007). doi:10.1038/nmat1849.

[14] K. S. Novoselov, A. K. Geim, S. V. Morozov, D. Jiang, M. I. Katsnelson, I. V. Grigorieva, S. V. Dubonos, and A. A. Firsov, *Two-dimensional gas of massless Dirac fermions in graphene*, Nature **438**, 197 (2005). doi:10.1038/nature04233.

[15] H. Shi, R. Yan, S. Bertolazzi, J. Brivio, B. Gao, A. Kis, D. Jena, H. G. Xing, and L. Huang, *Exciton Dynamics in Suspended Monolayer and Few-Layer MoS_2 2D Crystals*, ACS Nano **7**, 1072 (2013). doi:10.1021/nn303973r.

[16] T. Olsen, S. Latini, F. Rasmussen, and K. S. Thygesen, *Simple Screened Hydrogen Model of Excitons in Two-Dimensional Materials*, Physical Review Letters **116**, 056401 (2016). doi:10.1103/PhysRevLett.116.056401.

[17] H. Yu, G.-B. Liu, J. Tang, X. Xu, and W. Yao, *Moiré excitons: From programmable quantum emitter arrays to spin-orbit coupled artificial lattices*, Science Advances **3**, e1701696 (2017). doi:10.1126/sciadv.1701696.

[18] M. Kira and S. W. Koch, *Semiconductor Quantum Optics* (Cambridge University Press, 2011). doi:10.1017/CBO9781139016926.

[19] J. Zaanen, G. A. Sawatzky, and J. W. Allen, *Band gaps and electronic structure of transition-metal compounds*, Physical Review Letters **55**, 418 (1985). doi:10.1103/PhysRevLett.55.418.

[20] J. B. Torrance, P. Lacorre, C. Asavaroengchai, and R. M. Metzger, *Why are some oxides metallic, while most are insulating?*, Physica C: Superconductivity **182**, 351 (1991). doi:10.1016/0921-4534(91)90534-6.

[21] A. Klein, *Energy band alignment at interfaces of semiconducting oxides: A review of experimental determination using photoelectron spectroscopy and comparison with theoretical predictions by the electron affinity rule, charge neutrality levels, and the common anion rule*, Thin Solid Films **520**, 3721 (2012). doi:10.1016/j.tsf.2011.10.055.

[22] S.-H. Wei and A. Zunger, *Calculated natural band offsets of all II–VI and III–V semiconductors: Chemical trends and the role of cation d orbitals*, Applied Physics Letters **72**, 2011 (1998). doi:10.1063/1.121249.

[23] J. Y. Tsao, S. Chowdhury, M. A. Hollis, D. Jena, N. M. Johnson, K. A. Jones, R. J. Kaplar, S. Rajan, C. G. Van de Walle, E. Bellotti, C. L. Chua, R. Collazo, M. E. Coltrin, J. A. Cooper, K. R. Evans, S. Graham, T. A. Grotjohn, E. R. Heller, M. Higashiwaki, M. S. Islam, P. W. Juodawlkis, M. A. Khan, A. D. Koehler, J. H. Leach, U. K. Mishra, R. J. Nemanich, R. C. N. Pilawa-Podgurski, J. B. Shealy, Z. Sitar, M. J. Tadjer, A. F. Witulski, M. Wraback, and J. A. Simmons, *Ultrawide-Bandgap Semiconductors: Research Opportunities and Challenges*, Advanced Electronic Materials **4**, 1600501 (2018). doi:10.1002/aelm.201600501.

[24] A. Prakash, P. Xu, A. Faghaninia, S. Shukla, J. W. Ager, C. S. Lo, and B. Jalan, *Wide bandgap $BaSnO3$ films with room temperature conductivity exceeding 104 S cm−1*, Nature Communications **8**, 15167 (2017). doi:10.1038/ncomms15167.

[25] M. Grundmann, H. Frenzel, A. Lajn, M. Lorenz, F. Schein, and H. von Wenckstern, *Transparent semiconducting oxides: materials and devices*, physica status solidi (a) **207**, 1437 (2010). doi:https://doi.org/10.1002/pssa.200983771.

[26] E. Fortunato and R. Martins, *Where science fiction meets reality? With oxide semiconductors!*, physica status solidi (RRL) – Rapid Research Letters **5**, 336 (2011). doi:https://doi.org/10.1002/pssr.201105246.

[27] P. Ágoston, K. Albe, R. M. Nieminen, and M. J. Puska, *Intrinsic n-Type Behavior in Transparent Conducting Oxides: A Comparative Hybrid-Functional Study of In_2O_3, SnO_2, and ZnO*, Physical Review Letters **103**, 245501 (2009). doi:10.1103/PhysRevLett.103.245501.

[28] K. H. L. Zhang, K. Xi, M. G. Blamire, and R. G. Egdell, *P-type transparent conducting oxides*, Journal of Physics: Condensed Matter **28**, 383002 (2016). doi:10.1088/0953-8984/28/38/383002.

[29] H. Hosono and K. Ueda, *Transparent Conductive Oxides*. In S. Kasap and P. Capper, eds., *Springer Handbook of Electronic and Photonic Materials* (Cham: Springer International Publishing, 2017).

[30] J. B. Varley, A. Janotti, C. Franchini, and C. G. Van de Walle, *Role of self-trapping in luminescence and p-type conductivity of wide-band-gap oxides*, Physical Review B **85**, 081109 (2012). doi:10.1103/PhysRevB.85.081109.

[31] S. B. Zhang, S.-H. Wei, and A. Zunger, *Intrinsic n-type versus p-type doping asymmetry and the defect physics of ZnO*, Physical Review B **63**, 075205 (2001). doi:10.1103/PhysRevB.63.075205.

[32] Y. Youn, M. Lee, D. Kim, J. K. Jeong, Y. Kang, and S. Han, *Large-Scale Computational Identification of p-Type Oxide Semiconductors by Hierarchical Screening*, Chemistry of Materials **31**, 5475 (2019). doi:10.1021/acs.chemmater.9b00816.

[33] H. Kawazoe, M. Yasukawa, H. Hyodo, M. Kurita, H. Yanagi, and H. Hosono, *P-type electrical conduction in transparent thin films of $CuAlO_2$*, Nature **389**, 939 (1997). doi:10.1038/40087.

[34] N. Zheludev, *The life and times of the LED — a 100-year history*, Nature Photonics **1**, 189 (2007). doi:10.1038/nphoton.2007.34.

[35] N. Holonyak and S. F. Bevacqua, *Coherent (visible) light emission from $Ga(As_{1-x}P_x)$ junctions*, Applied Physics Letters **1**, 82 (1962). doi:10.1063/1.1753706.

[36] Y. Nanishi, *The birth of the blue LED*, Nature Photonics **8**, 884 (2014). doi:10.1038/nphoton.2014.291.

[37] E. F. Schubert and J. K. Kim, *Solid-State Light Sources Getting Smart*, Science **308**, 1274 (2005). doi:10.1126/science.1108712.

[38] S. Ye, F. Xiao, Y. Pan, Y. Ma, and Q. Zhang, *Phosphors in phosphor-converted white light-emitting diodes: Recent advances in materials, techniques and properties*, Materials Science and Engineering: R: Reports **71**, 1 (2010). doi:10.1016/j.mser.2010.07.001.

[39] W. Yen, M. Raukas, S. Basun, W. van Schaik, and U. Happek, *Optical and photoconductive properties of cerium-doped crystalline solids*, Journal of Luminescence **69**, 287 (1996). doi:10.1016/S0022-2313(96)00107-X.

[40] Y. Ma, L. Zhang, T. Zhou, B. Sun, Y. Wang, J. Kang, P. Gao, J. Huang, F. A. Selim, C. Wong, M. Li, and H. Chen, *High recorded color rendering index in single Ce,(Pr,Mn):YAG transparent ceramics for high-power white LEDs/LDs*, Journal of Material Chemistry C **8**, 4329 (2020). doi:10.1039/D0TC00032A.

[41] C. Becher, A. Kiraz, P. Michler, A. Imamoğlu, W. V. Schoenfeld, P. M. Petroff, L. Zhang, and E. Hu, *Nonclassical radiation from a single self-assembled InAs quantum dot*, Physical Review B **63**, 121312 (2001). doi:10.1103/PhysRevB.63.121312.

[42] C. Kurtsiefer, S. Mayer, P. Zarda, and H. Weinfurter, *Stable Solid-State Source of Single Photons*, Physical Review Letters **85**, 290 (2000). doi:10.1103/PhysRevLett.85.290.

[43] R. Loudon, *Photon Bunching and Antibunching*, Physics Bulletin **27**, 21 (1976). doi:10.1088/0031-9112/27/1/023.

[44] B. Lienhard, T. Schröder, S. Mouradian, F. Dolde, T. T. Tran, I. Aharonovich, and D. Englund, *Bright and photostable single-photon emitter in silicon carbide*, Optica **3**, 768 (2016). doi:10.1364/OPTICA.3.000768.

[45] A. Beveratos, R. Brouri, T. Gacoin, A. Villing, J.-P. Poizat, and P. Grangier, *Single Photon Quantum Cryptography*, Physical Review Letters **89**, 187901 (2002). doi:10.1103/PhysRevLett.89.187901.

[46] M. Berthel, O. Mollet, G. Dantelle, T. Gacoin, S. Huant, and A. Drezet, *Photophysics of single nitrogen-vacancy centers in diamond nanocrystals*, Physical Review B **91**, 035308 (2015). doi:10.1103/PhysRevB.91.035308.

[47] X. Cao, M. Zopf, and F. Ding, *Telecom wavelength single photon sources*, Journal of Semiconductors **40**, 071901 (2019). doi:10.1088/1674-4926/40/7/071901.

[48] G. R. Fisher and P. Barnes, *Towards a unified view of polytypism in silicon carbide*, Philosophical Magazine B **61**, 217 (1990). doi:10.1080/13642819008205522.

[49] H. J. von Bardeleben, J. L. Cantin, E. Rauls, and U. Gerstmann, *Identification and magneto-optical properties of the NV center in $4H$ − SiC*, Physical Review B **92**, 064104 (2015). doi:10.1103/PhysRevB.92.064104.

[50] S. I. Sato, T. Narahara, S. Onoda, Y. Yamazaki, Y. Hijikata, B. C. Gibson, A. Greentree, and T. Ohshima, *Near Infrared Photoluminescence of NCVSi- Centers in High-Purity Semi-Insulating 4H-SiC Irradiated with Energetic Charged Particles*, in *Silicon Carbide and Related Materials 2019*, vol. 1004 of *Materials Science Forum*, 355, Trans Tech Publications Ltd, 2020. doi:10.4028/www.scientific.net/MSF.1004.355.

[51] S. Castelletto, B. C. Johnson, V. Ivády, N. Stavrias, T. Umeda, A. Gali, and T. Ohshima, *A silicon carbide room-temperature single-photon source*, Nature Materials **13**, 151 (2014). doi:10.1038/nmat3806.

[52] V. L. Solozhenko, V. Z. Turkevich, and W. B. Holzapfel, *Refined Phase Diagram of Boron Nitride*, The Journal of Physical Chemistry B **103**, 2903 (1999). doi:10.1021/jp984682c.

[53] M. R. Rosenberger, C. K. Dass, H.-J. Chuang, S. V. Sivaram, K. M. McCreary, J. R. Hendrickson, and B. T. Jonker, *Quantum Calligraphy: Writing Single-Photon Emitters in a Two-Dimensional Materials Platform*, ACS Nano **13**, 904 (2019). doi:10.1021/acsnano.8b08730.

[54] Z. Shotan, H. Jayakumar, C. R. Considine, M. Mackoit, H. Fedder, J. Wrachtrup, A. Alkauskas, M. W. Doherty, V. M. Menon, and C. A. Meriles, *Photoinduced Modification of Single-Photon Emitters in Hexagonal Boron Nitride*, ACS Photonics **3**, 2490 (2016). doi:10.1021/acsphotonics.6b00736.

[55] R. Bourrellier, S. Meuret, A. Tararan, O. Stéphan, M. Kociak, L. H. G. Tizei, and A. Zobelli, *Bright UV Single Photon Emission at Point Defects in h-BN*, Nano Letters **16**, 4317 (2016). doi:10.1021/acs.nanolett.6b01368.

[56] A. D. Oyedele, S. Yang, L. Liang, A. A. Puretzky, K. Wang, J. Zhang, P. Yu, P. R. Pudasaini, A. W. Ghosh, Z. Liu, C. M. Rouleau, B. G. Sumpter, M. F. Chisholm, W. Zhou,

P. D. Rack, D. B. Geohegan, and K. Xiao, *PdSe$_2$: Pentagonal Two-Dimensional Layers with High Air Stability for Electronics*, Journal of the American Chemical Society **139**, 14090 (2017). doi:10.1021/jacs.7b04865.

[57]   A. Stukowski, *Visualization and analysis of atomistic simulation data with OVITO–the Open Visualization Tool*, Modelling and Simulation in Materials Science and Engineering **18**, 015012 (2009). doi:10.1088/0965-0393/18/1/015012.

[58]   S. Haastrup, M. Strange, M. Pandey, T. Deilmann, P. S. Schmidt, N. F. Hinsche, M. N. Gjerding, D. Torelli, P. M. Larsen, A. C. Riis-Jensen, J. Gath, K. W. Jacobsen, J. J. Mortensen, T. Olsen, and K. S. Thygesen, *The Computational 2D Materials Database: high-throughput modeling and discovery of atomically thin crystals*, 2D Materials **5**, 042002 (2018). doi:10.1088/2053-1583/aacfc1.

[59]   M. N. Gjerding, A. Taghizadeh, A. Rasmussen, S. Ali, F. Bertoldo, T. Deilmann, N. R. Knøsgaard, M. Kruse, A. H. Larsen, S. Manti, T. G. Pedersen, U. Petralanda, T. Skovhus, M. K. Svendsen, J. J. Mortensen, T. Olsen, and K. S. Thygesen, *Recent progress of the Computational 2D Materials Database (C2DB)*, 2D Materials **8**, 044002 (2021). doi:10.1088/2053-1583/ac1059.

[60]   R. G. Dickinson and L. Pauling, *THE CRYSTAL STRUCTURE OF MOLYBDENITE*, Journal of the American Chemical Society **45**, 1466 (1923). doi:10.1021/ja01659a020.

[61]   J. Gusakova, X. Wang, L. L. Shiau, A. Krivosheeva, V. Shaposhnikov, V. Borisenko, V. Gusakov, and B. K. Tay, *Electronic Properties of Bulk and Monolayer TMDs: Theoretical Study Within DFT Framework (GVJ-2e Method)*, physica status solidi (a) **214**, 1700218 (2017). doi:10.1002/pssa.201700218.

[62]   H. Li, J. Wu, Z. Yin, and H. Zhang, *Preparation and Applications of Mechanically Exfoliated Single-Layer and Multilayer MoS$_2$ and WSe$_2$ Nanosheets*, Accounts of Chemical Research **47**, 1067 (2014). doi:10.1021/ar4002312.

[63]   Y.-H. Lee, X.-Q. Zhang, W. Zhang, M.-T. Chang, C.-T. Lin, K.-D. Chang, Y.-C. Yu, J. T.-W. Wang, C.-S. Chang, L.-J. Li, and T.-W. Lin, *Synthesis of Large-Area MoS$_2$ Atomic Layers with Chemical Vapor Deposition*, Advanced Materials **24**, 2320 (2012). doi:https://doi.org/10.1002/adma.201104798.

[64]   D. O. Lindroth and P. Erhart, *Thermal transport in van der Waals solids from first-principles calculations*, Physical Review B **94**, 115205 (2016). doi:10.1103/PhysRevB.94.115205.

[65]   C. Gong, H. Zhang, W. Wang, L. Colombo, R. M. Wallace, and K. Cho, *Band alignment of two-dimensional transition metal dichalcogenides: Application in tunnel field effect transistors*, Applied Physics Letters **103**, 053513 (2013). doi:10.1063/1.4817409.

[66]   M. Kuisma, J. Ojanen, J. Enkovaara, and T. T. Rantala, *Kohn-Sham potential with discontinuity for band gap materials*, Physical Review B **82**, 115106 (2010). doi:10.1103/PhysRevB.82.115106.

[67]   D. Y. Qiu, F. H. da Jornada, and S. G. Louie, *Optical Spectrum of MoS$_2$: Many-Body Effects and Diversity of Exciton States*, Physical Review Letters **111**, 216805 (2013). doi:10.1103/PhysRevLett.111.216805.

[68] W. Shan, B. D. Little, A. J. Fischer, J. J. Song, B. Goldenberg, W. G. Perry, M. D. Bremser, and R. F. Davis, *Binding energy for the intrinsic excitons in wurtzite GaN*, Physical Review B **54**, 16369 (1996). doi:10.1103/PhysRevB.54.16369.

[69] B. Sklénard, A. Dragoni, F. Triozon, and V. Olevano, *Optical vs electronic gap of hafnia by ab initio Bethe-Salpeter equation*, Applied Physics Letters **113**, 172903 (2018). doi:10.1063/1.5044631.

[70] T. Cheiwchanchamnangij and W. R. L. Lambrecht, *Quasiparticle band structure calculation of monolayer, bilayer, and bulk MoS_2*, Physical Review B **85**, 205302 (2012). doi:10.1103/PhysRevB.85.205302.

[71] K. Berland and P. Hyldgaard, *Exchange functional that tests the robustness of the plasmon description of the van der Waals density functional*, Physical Review B **89**, 035412 (2014). doi:10.1103/PhysRevB.89.035412.

[72] Y. Cao, V. Fatemi, S. Fang, K. Watanabe, T. Taniguchi, E. Kaxiras, and P. Jarillo-Herrero, *Unconventional superconductivity in magic-angle graphene superlattices*, Nature **556**, 43 (2018). doi:10.1038/nature26160.

[73] L. Xian, D. M. Kennes, N. Tancogne-Dejean, M. Altarelli, and A. Rubio, *Multiflat Bands and Strong Correlations in Twisted Bilayer Boron Nitride: Doping-Induced Correlated Insulator and Superconductor*, Nano Letters **19**, 4934 (2019). doi:10.1021/acs.nanolett.9b00986.

[74] M. H. Naik and M. Jain, *Ultraflatbands and Shear Solitons in Moiré Patterns of Twisted Bilayer Transition Metal Dichalcogenides*, Physical Review Letters **121**, 266401 (2018). doi:10.1103/PhysRevLett.121.266401.

[75] S. Shallcross, S. Sharma, and O. A. Pankratov, *Quantum Interference at the Twist Boundary in Graphene*, Physical Review Letters **101**, 056803 (2008). doi:10.1103/PhysRevLett.101.056803.

[76] K. Hermann, *Periodic overlayers and moiré patterns: theoretical studies of geometric properties*, Journal of Physics: Condensed Matter **24**, 314210 (2012). doi:10.1088/0953-8984/24/31/314210.

[77] J. M. B. Lopes dos Santos, N. M. R. Peres, and A. H. Castro Neto, *Graphene Bilayer with a Twist: Electronic Structure*, Physical Review Letters **99**, 256802 (2007). doi:10.1103/PhysRevLett.99.256802.

[78] B. Alling, A. V. Ruban, A. Karimi, O. E. Peil, S. I. Simak, L. Hultman, and I. A. Abrikosov, *Mixing and decomposition thermodynamics of $c-Ti_{1-x}Al_xN$ from first-principles calculations*, Physical Review B **75**, 045123 (2007). doi:10.1103/PhysRevB.75.045123.

[79] M. Ångqvist, W. A. Muñoz, J. M. Rahm, E. Fransson, C. Durniak, P. Rozyczko, T. H. Rod, and P. Erhart, *ICET – A Python Library for Constructing and Sampling Alloy Cluster Expansions*, Adv Theo. Simul. **2**, 1900015 (2019). doi:10.1002/adts.201900015.

[80] C. G. Van de Walle and J. Neugebauer, *First-principles calculations for defects and impurities: Applications to III-nitrides*, Journal of Applied Physics **95**, 3851 (2004). doi:10.1063/1.1682673.

[81] S. Harada, K. Tanaka, and H. Inui, *Thermoelectric properties and crystallographic shear structures in titanium oxides of the Magnèli phases*, Journal of Applied Physics **108**, 083703 (2010). doi:10.1063/1.3498801.

[82]   S. B. Zhang and J. E. Northrup, *Chemical potential dependence of defect formation energies in GaAs: Application to Ga self-diffusion,* Physical Review Letters **67**, 2339 (1991). doi:10.1103/PhysRevLett.67.2339.

[83]   J. P. Perdew, A. Ruzsinszky, G. I. Csonka, O. A. Vydrov, G. E. Scuseria, L. A. Constantin, X. Zhou, and K. Burke, *Restoring the Density-Gradient Expansion for Exchange in Solids and Surfaces,* Physical Review Letters **100**, 136406 (2008). doi:10.1103/PhysRevLett.100.136406.

[84]   M. Fox, *Optical Properties of Solids* (OUP Oxford, 2010). ISBN 9780199573363.

[85]   V. Barone, J. Bloino, M. Biczysko, and F. Santoro, *Fully Integrated Approach to Compute Vibrationally Resolved Optical Spectra: From Small Molecules to Macrosystems,* Journal of Chemical Theory and Computation **5**, 540 (2009). doi:10.1021/ct8004744.

[86]   A. Baiardi, J. Bloino, and V. Barone, *General time dependent approach to vibronic spectroscopy including franck-condon, herzberg-teller, and duschinsky effects,* Journal of Chemical Theory and Computation **9**, 4097 (2013). doi:10.1021/ct400450k.

[87]   G. Mahan, *Many-Particle Physics* (Springer US, 2000). ISBN 9780306463389.

[88]   T. Miyakawa and D. L. Dexter, *Phonon Sidebands, Multiphonon Relaxation of Excited States, and Phonon-Assisted Energy Transfer between Ions in Solids,* Physical Review B **1**, 2961 (1970). doi:10.1103/PhysRevB.1.2961.

[89]   R. Kubo and Y. Toyozawa, *Application of the Method of Generating Function to Radiative and Non-Radiative Transitions of a Trapped Electron in a Crystal,* Progress of Theoretical Physics **13**, 160 (1955). doi:10.1143/ptp.13.160.

[90]   J. J. Markham, *Interaction of Normal Modes with Electron Traps,* Reviews of Modern Physics **31**, 956 (1959). doi:10.1103/RevModPhys.31.956.

[91]   A. Kelley, *Condensed-Phase Molecular Spectroscopy and Photophysics* (Wiley, 2012). ISBN 9781118493069.

[92]   P. Hohenberg and W. Kohn, *Inhomogeneous Electron Gas,* Physical Review **136**, B864 (1964). doi:10.1103/PhysRev.136.B864.

[93]   R. M. Martin, *Electronic Structure: Basic Theory and Practical Methods* (Cambridge University Press, 2004). doi:10.1017/CBO9780511805769.

[94]   W. Kohn and L. J. Sham, *Self-Consistent Equations Including Exchange and Correlation Effects,* Physical Review **140**, A1133 (1965). doi:10.1103/PhysRev.140.A1133.

[95]   J. Sun, A. Ruzsinszky, and J. P. Perdew, *Strongly Constrained and Appropriately Normed Semilocal Density Functional,* Physical Review Letters **115**, 036402 (2015). doi:10.1103/PhysRevLett.115.036402.

[96]   J. P. Perdew and K. Schmidt, *Jacob's ladder of density functional approximations for the exchange-correlation energy,* AIP Conference Proceedings **577**, 1 (2001). doi:10.1063/1.1390175.

[97]   D. M. Ceperley and B. J. Alder, *Ground State of the Electron Gas by a Stochastic Method,* Physical Review Letters **45**, 566 (1980). doi:10.1103/PhysRevLett.45.566.

[98]   J. P. Perdew and Y. Wang, *Accurate and simple analytic representation of the electron-gas correlation energy,* Physical Review B **45**, 13244 (1992). doi:10.1103/PhysRevB.45.13244.

[99]   J. P. Perdew, K. Burke, and M. Ernzerhof, *Generalized Gradient Approximation Made Simple,* Physical Review Letters **77**, 3865 (1996). doi:10.1103/PhysRevLett.77.3865.

[100] M. Dion, H. Rydberg, E. Schröder, D. C. Langreth, and B. I. Lundqvist, *Van der Waals Density Functional for General Geometries*, Physical Review Letters **92**, 246401 (2004). doi: 10.1103/PhysRevLett.92.246401.

[101] L. Gharaee, P. Erhart, and P. Hyldgaard, *Finite-temperature properties of nonmagnetic transition metals: Comparison of the performance of constraint-based semilocal and nonlocal functionals*, Physical Review B **95**, 085147 (2017). doi:10.1103/PhysRevB.95.085147.

[102] J. P. Perdew and A. Zunger, *Self-interaction correction to density-functional approximations for many-electron systems*, Physical Review B **23**, 5048 (1981). doi:10.1103/PhysRevB.23.5048.

[103] J. P. Perdew, M. Ernzerhof, and K. Burke, *Rationale for mixing exact exchange with density functional approximations*, The Journal of Chemical Physics **105**, 9982 (1996). doi:10.1063/1.472933.

[104] J. Heyd, G. E. Scuseria, and M. Ernzerhof, *Hybrid functionals based on a screened Coulomb potential*, The Journal of Chemical Physics **118**, 8207 (2003). doi:10.1063/1.1564060.

[105] J. Heyd, G. E. Scuseria, and M. Ernzerhof, *Erratum: "Hybrid functionals based on a screened Coulomb potential" [Journal of Chemical Physics **118**, 8207 (2003)]*, The Journal of Chemical Physics **124**, 219906 (2006). doi:10.1063/1.2204597.

[106] G. Makov and M. C. Payne, *Periodic boundary conditions in ab initio calculations*, Physical Review B **51**, 4014 (1995). doi:10.1103/PhysRevB.51.4014.

[107] S. Lany and A. Zunger, *Assessment of correction methods for the band-gap problem and for finite-size effects in supercell defect calculations: Case studies for ZnO and GaAs*, Physical Review B **78**, 235104 (2008). doi:10.1103/PhysRevB.78.235104.

[108] H.-P. Komsa, N. Berseneva, A. V. Krasheninnikov, and R. M. Nieminen, *Charged Point Defects in the Flatland: Accurate Formation Energy Calculations in Two-Dimensional Materials*, Physical Review X **4**, 031044 (2014). doi:10.1103/PhysRevX.4.031044.

[109] H.-P. Komsa, N. Berseneva, A. V. Krasheninnikov, and R. M. Nieminen, *Erratum: Charged Point Defects in the Flatland: Accurate Formation Energy Calculations in Two-Dimensional Materials [Physical Review X **4**, 031044 (2014)]*, Physical Review X **8**, 039902 (2018). doi:10.1103/PhysRevX.8.039902.

[110] P. Erhart, B. Sadigh, A. Schleife, and D. Åberg, *First-principles study of codoping in lanthanum bromide*, Physical Review B **91**, 165206 (2015). doi:10.1103/PhysRevB.91.165206.

[111] P. E. Blöchl, *Projector augmented-wave method*, Physical Review B **50**, 17953 (1994). doi:10.1103/PhysRevB.50.17953.

[112] C. Rostgaard, *The Projector Augmented-wave Method*, 2009. arxiv/0910.1921.

[113] J. J. Mortensen, L. B. Hansen, and K. W. Jacobsen, *Real-space grid implementation of the projector augmented wave method*, Physical Review B **71**, 035109 (2005). doi:10.1103/PhysRevB.71.035109.

[114] J. Enkovaara, C. Rostgaard, J. J. Mortensen, J. Chen, M. Dułak, L. Ferrighi, J. Gavnholt, C. Glinsvad, V. Haikola, H. A. Hansen, H. H. Kristoffersen, M. Kuisma, A. H. Larsen, L. Lehtovaara, M. Ljungberg, O. Lopez-Acevedo, P. G. Moses, J. Ojanen, T. Olsen, V. Petzold, N. A. Romero, J. Stausholm-Møller, M. Strange, G. A. Tritsaris, M. Vanin, M. Walter, B. Hammer, H. Häkkinen, G. K. H. Madsen, R. M. Nieminen, J. K. Nørskov, M. Puska,

T. T. Rantala, J. Schiøtz, K. S. Thygesen, and K. W. Jacobsen, *Electronic structure calculations with GPAW: a real-space implementation of the projector augmented-wave method*, Journal of Physics: Condensed Matter **22**, 253202 (2010). doi:10.1088/0953-8984/22/25/253202.

[115] G. Kresse and J. Hafner, *Ab initio molecular dynamics for liquid metals*, Physical Review B **47**, 558 (1993). doi:10.1103/PhysRevB.47.558.

[116] G. Kresse and J. Furthmüller, *Efficiency of ab-initio total energy calculations for metals and semiconductors using a plane-wave basis set*, Computational Materials Science **6**, 15 (1996). doi:10.1016/0927-0256(96)00008-0.

[117] G. Kresse and J. Furthmüller, *Efficient iterative schemes for ab initio total-energy calculations using a plane-wave basis set*, Physical Review B **54**, 11169 (1996). doi:10.1103/PhysRevB.54.11169.

[118] L. Hedin, *New Method for Calculating the One-Particle Green's Function with Application to the Electron-Gas Problem*, Physical Review **139**, A796 (1965). doi:10.1103/PhysRev.a139.A796.

[119] F. Aryasetiawan and O. Gunnarsson, *The GW method*, Reports on Progress in Physics **61**, 237 (1998). doi:10.1088/0034-4885/61/3/002.

[120] A. Szabo and N. S. Ostlund, *Modern Quantum Chemistry: Introduction to Advanced Electronic Structure Theory* (Dover Publications, 1996). ISBN 9780486691862.

[121] X.-Z. Li, R. Gómez-Abal, H. Jiang, C. Ambrosch-Draxl, and M. Scheffler, *Impact of widely used approximations to the G_0W_0 method: an all-electron perspective*, New Journal of Physics **14**, 023006 (2012). doi:10.1088/1367-2630/14/2/023006.

[122] F. Caruso, P. Rinke, X. Ren, M. Scheffler, and A. Rubio, *Unified description of ground and excited states of finite systems: The self-consistent GW approach*, Physical Review B **86**, 081102 (2012). doi:10.1103/PhysRevB.86.081102.

[123] K. Andersen, S. Latini, and K. S. Thygesen, *Dielectric Genome of van der Waals Heterostructures*, Nano Letters **15**, 4616 (2015). doi:10.1021/acs.nanolett.5b01251.

[124] D. Y. Qiu, F. H. da Jornada, and S. G. Louie, *Screening and many-body effects in two-dimensional crystals: Monolayer MoS_2*, Physical Review B **93**, 235435 (2016). doi:10.1103/PhysRevB.93.235435.

[125] R. Ouyang, S. Curtarolo, E. Ahmetcik, M. Scheffler, and L. M. Ghiringhelli, *SISSO: A compressed-sensing method for identifying the best low-dimensional descriptor in an immensity of offered candidates*, Physical Review Materials **2**, 083802 (2018). doi:10.1103/PhysRevMaterials.2.083802.

[126] J. Schmidt, M. R. G. Marques, S. Botti, and M. A. L. Marques, *Recent advances and applications of machine learning in solid-state materials science*, npj Computational Materials **5**, 83 (2019). doi:10.1038/s41524-019-0221-0.

[127] L. Shi, K. Xu, and L.-W. Wang, *Comparative study of ab initio nonradiative recombination rate calculations under different formalisms*, Physical Review B **91**, 205315 (2015). doi:10.1103/PhysRevB.91.205315.